


Tutorial on Superconducting Quantum Circuits: From Basics to Applications

Denys Derlian Carvalho Brito ¹, Fernando Valadares ² and André Jorge Carvalho Chaves (corresponding author) ^{1,3}

¹*Departamento de Física, Instituto Tecnológico de Aeronáutica, Praça Marechal Eduardo Gomes, São José dos Campos, 12228-900, São Paulo, Brasil.*

²*Centre for Quantum Technologies, National University of Singapore, Lower Kent Ridge Rd, Queenstown, 119077, Singapore*

³*Centro de Física (CF-UM-UP) and Departamento de Física, Universidade do Minho, P-4710-057 Braga, Portugal*

(*Electronic mail: andrejck@ita.br)

(*Electronic mail: fernando.valadares@u.nus.edu)

(*Electronic mail: derlian@ita.com)

(Dated: 23 October 2025)

As superconducting circuits emerge as a leading platform for scalable quantum information processing, building comprehensive bridges from the foundational principles of macroscopic quantum phenomena to the architecture of modern quantum devices is increasingly essential for introducing new researchers to the field. This tutorial provides a self-contained, pedagogical introduction to superconducting quantum circuits at the undergraduate level. Beginning with an overview of superconductivity and the Josephson effect, the tutorial systematically develops the quantization of microwave circuits into the framework of circuit quantum electrodynamics (cQED). The transmon qubit is then introduced as a state-of-the-art application, with a detailed derivation of its Hamiltonian and its interaction with control and read-out circuitry. The theoretical formalism is consolidated through a numerical simulation of vacuum Rabi oscillations in a driven transmon-resonator system, a canonical experiment that demonstrates the coherent energy exchange characteristic of the strong coupling regime. This work serves as a foundational guide and first point of contact, equipping students and researchers with the conceptual and mathematical tools necessary to understand and engineer superconducting quantum hardware.

CONTENTS

I. Introduction	2	A. Transmon-Resonator Coupling	16
II. Superconductivity	2	1. Transmon coupled to gate voltage	16
A. Classical Formulation	3	2. Transmon coupled to resonator	17
1. Perfect conductivity	3	B. Rotating frames and approximations	18
2. Meissner effect	4	1. Displaced Frame	19
B. Quantum Formulation	5	C. Jaynes-Cummings Spectrum	20
1. Supercurrent Equation	5	D. Drives and driven systems	21
2. London Equations	6	1. Drive connected to a quantum system	22
III. Josephson Effect	7	2. Dispersive Readout	23
A. DC Josephson Effect	7	VI. Application Example: Rabi Oscillations in a Driven Transmon-Resonator System	25
Connection to Superconducting Phase and Magnetic Flux	8	A. System Configuration and Parameters	25
Derivation of the DC Josephson Relation	9	B. Experimental Protocol and Simulation Scenarios	25
Physical Interpretation	9	C. Hamiltonian and Dissipative Dynamics	25
B. AC Josephson Effect	9	D. Measurement	26
IV. Circuit Quantum Electrodynamics	10	E. Transmon Excitation via Coherent Drive	26
A. Microwave Resonators	10	F. Simplified Experimental Setup	26
1. Classical Resonator	10	G. System Evolution — Results and Discussion	27
2. Quantum Resonator – Simple Formulation	11	1. System Baseline Behavior	27
3. Quantum Resonator – Transmission Line	12	2. Vacuum Rabi Oscillations Measurement	27
B. Practical Examples of Microwave Resonators	14	VII. Conclusion	28
V. Transmons	14	Funding	28
		References	28

References 28

A. Quantum Harmonic Oscillator	30
1. Energy and Important Operators	30
2. Time Evolution of a Quantum Harmonic Oscillator	31
3. Coherent States	31
B. Langevin Equation and Input-Output Theory	32

I. INTRODUCTION

Quantum technologies, including quantum computing, quantum sensing, and quantum communication, are at the forefront of what is commonly referred to as the “Second Quantum Revolution”¹. This emerging paradigm arises from the intersection of quantum mechanics and information science, which forms the foundation of Quantum Information Science (QIS)². Quantum computing, in particular, has garnered significant attention due to its potential to solve certain computational problems exponentially faster than classical approaches^{3,4}. Applications of this technology span numerous domains, including scientific research, industrial innovation, national security, and real-time data processing^{3,5,6}.

Among the leading physical implementations of quantum processors, superconducting qubits have emerged as a highly promising platform^{7–12}. These systems offer key advantages such as compatibility with microwave control technologies, integration with existing lithographic and electronic techniques, and scalability to multi-qubit architectures^{13,14}. Their operation at cryogenic temperatures **helps reduce** energy dissipation and **thermal noise, contributing to** extended coherence times—both essential for the reliable execution of quantum algorithms and the realization of fault-tolerant quantum computing¹⁵.

Given their unique properties, superconducting qubits are positioned as a cornerstone of emerging quantum computing architectures. Their utility extends beyond computational applications to encompass secure communication systems and advanced sensing platforms^{16,17}. A comprehensive understanding of their physical principles, design considerations, and control mechanisms is thus essential for researchers and engineers engaged in the development of practical quantum technologies.

However, for students and researchers entering the field, the path from the underlying physics to a functional quantum device can be daunting, as it requires synthesizing concepts from condensed matter physics, quantum optics, and microwave engineering. A clear, pedagogical bridge from first principles to modern hardware is therefore essential for training the next generation of quantum engineers and scientists. This tutorial provides this bridge, starting from the basics of superconductivity to the introductory design and operation of a state-of-the-art transmon qubit. This tutorial is organized as follows: In Sec. II, we discuss the basics of superconductivity, including the Meissner effect and the London equation. In Sec. III, the Josephson effect is introduced; in Sec. IV, we present

some aspects of circuit quantum electrodynamics, which allow the definition of the transmon in Sec. V. Finally, in Sec. VI some applications are presented.

II. SUPERCONDUCTIVITY

The liquefaction of Helium, performed by H. Kamerlingh Onnes in 1908¹⁸, set the grounds for the investigation of physics at few-Kelvin temperatures, leading to the development of many cryogenic technologies in the subsequent decades¹⁹. In 1911, the phenomenon of superconductivity was observed for the first time with the abrupt fall of mercury’s resistivity below a *critical temperature* (T_c) of approximately 4.1 K²⁰, as shown in Fig. 1. **While a superconductor exhibits zero DC resistance like a perfect conductor, it was later demonstrated that superconductivity is a distinct physical phenomenon characterized by unique magnetic properties²¹.**

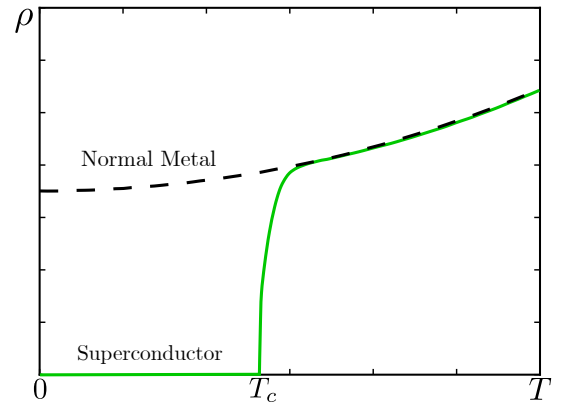


FIG. 1. Depiction of a superconducting metal resistivity curve *versus* temperature.

The distinction between a perfect conductor and a superconductor is that, while both exhibit zero electrical resistance below T_c , their interaction with magnetic fields is phenomenologically different. A perfect conductor would maintain a constant magnetic field in its interior; if cooled in the absence of a field and then exposed to one, it would exclude it, but if cooled in a pre-existing field, it would trap that field internally. A superconductor, in contrast, actively expels all magnetic flux from its interior when cooled below its critical temperature, regardless of the order of operations. This phenomenon of perfect diamagnetism is known as the **Meissner effect** and is a defining characteristic of superconductivity.

Superconductors can be further defined by their interaction with magnetic flux, being labeled as Type I or Type II. As a qualitative comparison, Type I superconductors completely exclude an applied magnetic flux via the Meissner effect up to a critical field H_c , at which point they transition to a normal, resistive state. In contrast, Type II superconductors exhibit two critical fields, H_{c1} and H_{c2} . Below H_{c1} , they behave like Type I superconductors, completely expelling the magnetic field. However, between H_{c1} and H_{c2} , the material enters a

"mixed state". In this state, the magnetic field penetrates the material in the form of discrete quantized channels known as **flux vortices**. Each vortex consists of a normal-state (resistive) core containing magnetic flux, which is surrounded by a circulating supercurrent that shields the rest of the material. This behavior can be visualized in Fig. 2.

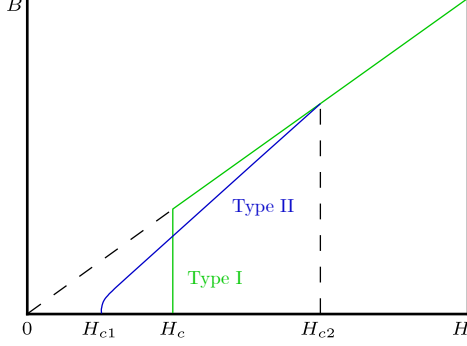


FIG. 2. Comparison of the magnetic response for Type I (green) and Type II (blue) superconductors. The plot shows the internal magnetic field (\mathbf{B}) versus the applied external field (\mathbf{H}). This characteristic behavior assumes a simple geometry, such as a long cylinder with a parallel applied field, to minimize complex effects arising from the sample's shape (demagnetization) and crystalline orientation.

For applications in superconducting quantum circuits, the choice of materials is a critical aspect. **Aluminum (Al)**, a Type I superconductor, remains the workhorse material for fabricating qubits¹¹. Its primary advantage lies not in its superconductor type, but in its ability to form a high-quality, self-limiting native oxide (AlOx), which serves as a reliable and reproducible insulating tunnel barrier for Al/AlOx/Al Josephson junctions²².

For other components like wiring and resonators, **Niobium (Nb)**, a Type II superconductor, is also frequently used¹¹. More recently, **Tantalum (Ta)**, a Type I material, has gained popularity for high-coherence qubits due to its favorable surface properties²³. However, the distinction between Type I and II behavior becomes less rigid for the thin films used in these devices. Even aluminum films can trap magnetic flux vortices, which can move and create magnetic noise, a significant source of decoherence^{24,25}. This makes meticulous magnetic shielding essential for all high-coherence circuits. Ultimately, qubit performance is limited by a combination of factors, including Two-Level System (TLS) defects, quasiparticles, dielectric loss, and trapped flux, rather than by the bulk superconductor type alone^{7,8,26}. Table I summarizes some common superconducting materials used in quantum circuits, along with their critical temperatures and types.

The phenomenological description of superconductors has deep implications for its microscopic behavior. In the next section, we explore how the perfect conductivity and the magnetic field expulsion, known as the *Meissner effect*, can be understood in terms of classical physics, and how they require the use of the quantum formalism for a complete description

in terms of the London equations.

A. Classical Formulation

We'll begin the quantitative development by using a classical formulation from Newtonian Laws and Maxwell equations in order to determine a general behavior pattern for a perfect superconductor.

1. Perfect conductivity

The linear relation between the electric field \mathbf{E} inside a conductor and the induced current density \mathbf{J} is quantified by the *conductivity* σ according to Ohm's law:

$$\mathbf{J} = \sigma \mathbf{E}. \quad (1)$$

At the microscopic level, this relation is understood as the result of the continuous scattering of electrons in the material as described by Drude's model. Perfect conductivity, however, assumes zero-resistivity, frictionless motion of the charge carriers, breaking this relation. From the second law of mechanics, the electrons of *mass* m and *charge magnitude* $e > 0$ freely accelerate in a field \mathbf{E} with a rate $\ddot{\mathbf{r}}$:

$$\mathbf{F} = m\ddot{\mathbf{r}} = -e\mathbf{E}. \quad (2)$$

The *current density* \mathbf{J} is related to the electron movement and density n_e as:

$$\mathbf{J} = -en_e\dot{\mathbf{r}} \rightarrow \dot{\mathbf{J}} = -en_e\ddot{\mathbf{r}}, \quad (3)$$

leading to the relation between \mathbf{J} and \mathbf{E}

$$\dot{\mathbf{J}} = \frac{n_e e^2}{m} \mathbf{E}. \quad (4)$$

This equation is in direct conflict with Ohm's law, since there is no stable value of \mathbf{J} for an $\mathbf{E} \neq 0$.

There are two immediate conclusions: first, since the current density diverges under the action of the electric field, we can understand perfect conductivity as the limit $\sigma \rightarrow \infty$. Second, as a consequence, the value of the electric field in the bulk of a perfect conductor must always be null for any finite current flow.

Perfect conductivity also has consequences on the dynamics of the *magnetic field* \mathbf{B} . According to Maxwell equations (Ampère's and Faraday's law, respectively)³⁰:

$$\nabla \times \mathbf{B} = \frac{4\pi}{c} \mathbf{J}, \quad (5)$$

$$\nabla \times \mathbf{E} = -\frac{1}{c} \frac{\partial \mathbf{B}}{\partial t}, \quad (6)$$

where we take the macroscopic average values of the fields, and c is the *speed of light*. From Eqs. (4) and (6):

$$\nabla \times \frac{\partial \mathbf{J}}{\partial t} = -\frac{n_e e^2}{cm} \frac{\partial \mathbf{B}}{\partial t}. \quad (7)$$

TABLE I. A selection of common superconducting materials with their respective critical temperatures (T_c) and type²⁷.

Material	Symbol	Critical Temp. (T_c)	Type	Notes
Aluminum	Al	1.2 K	I	Widely used for qubits and resonators ¹¹ .
Niobium	Nb	9.3 K	II	Borderline type; used for resonators and wiring ¹¹ .
Tantalum	Ta	4.5 K	I	Gaining popularity for high-coherence qubits ²³ .
Lead	Pb	7.2 K	I	A historically important elemental superconductor.
Mercury	Hg	4.2 K	I	The first superconductor discovered.
Niobium Nitride	NbN	~16 K	II	Used in Superconducting Single-Photon Detectors (SNSPDs) ²⁸ .
Niobium-Titanium	NbTi	~10 K	II	The workhorse wire for high-field superconducting magnets ²⁹ .
YBCO	-	~93 K	II	A common "high-temperature" superconductor.

On the other hand, the time derivative followed by the curl of Eq.(5) leads to:

$$\nabla \times \nabla \times \frac{\partial \mathbf{B}}{\partial t} = \frac{4\pi}{c} \nabla \times \frac{\partial \mathbf{J}}{\partial t}, \quad (8)$$

which, together with Eq. (7), gives:

$$\nabla \times \nabla \times \frac{\partial \mathbf{B}}{\partial t} = -\frac{4\pi n_e e^2}{mc^2} \frac{\partial \mathbf{B}}{\partial t}. \quad (9)$$

This expression can be simplified using the vector identity $\nabla \times \nabla \times = \nabla \nabla \cdot - \nabla^2$:

$$\nabla \frac{\partial}{\partial t} (\nabla \cdot \mathbf{B}) - \nabla^2 \frac{\partial \mathbf{B}}{\partial t} = -\frac{4\pi n_e e^2}{mc^2} \frac{\partial \mathbf{B}}{\partial t}, \quad (10)$$

resulting in the second-order partial differential equation on \mathbf{B} :

$$\nabla^2 \frac{\partial \mathbf{B}}{\partial t} = \frac{1}{\lambda^2} \frac{\partial \mathbf{B}}{\partial t}, \quad (11)$$

where λ is a function of the material parameters:

$$\lambda = \sqrt{\frac{mc^2}{4\pi n_e e^2}}. \quad (12)$$

When Eq. 12 is analyzed near the surface of the perfect conductor, there are two possible solutions given by $\frac{\partial \mathbf{B}}{\partial t} \propto e^{\pm z/\lambda}$, where z is the spatial coordinate penetrating the material. Neglecting the diverging solution, the conclusion is that the time-derivative of \mathbf{B} is exponentially suppressed in space with a characteristic penetration depth of λ , implying the magnetic field is constant in the bulk.

Although this description provides a good insight into the behavior of a perfect conductor, it is an incomplete representation of superconductors, as later experiments would reveal^{27,31}. In addition to having zero resistivity, superconductors also show perfect diamagnetism, expelling magnetic flux from their interior. This phenomenon, known as the Meissner effect, is one of the most distinctive properties of a superconductor.

2. Meissner effect

In 1933, Meissner and Oschenfeld observed an exclusion of the magnetic flux when a sphere is cooled below its transition

temperature^{31,32}. This discovery was relevant as it established the fundamental distinction between a superconductor and a hypothetical "perfect conductor". In their experiment, they measured the magnetic field distribution outside single-crystal samples of tin and lead. They observed that when the samples were cooled below their transition temperature while already in an external magnetic field, the magnetic flux was actively expelled from their interior³¹.

This perfect diamagnetism is a unique characteristic of the superconducting state and is not what would be expected from a perfect conductor, which would merely prevent any change in the internal magnetic field, thus trapping the field if cooled in its presence. The Meissner effect, therefore, revealed that superconductivity is a distinct thermodynamic phase and not simply a limit of classical electromagnetism.

Given the relation between *magnetic flux density* (\mathbf{H}), *magnetization* (\mathbf{M}) and *magnetic field* (\mathbf{B}), a null magnetic field requires, in Gaussian units:

$$\mathbf{B} = \mathbf{H} + 4\pi \mathbf{M}, \quad (13)$$

$$\mathbf{M} = -\frac{1}{4\pi} \mathbf{H}. \quad (14)$$

This relation implies the superconductor currents are rearranged so as to induce a magnetization \mathbf{M} that completely expels magnetic fields from the bulk of the material. This property, coupled with the expulsion of electric field given by perfect conductivity, has immediate applications in building effective shields to protect sensitive equipment from unwanted electromagnetic interference. Furthermore, the perfect diamagnetism can be utilized in magnetic levitation applications, where objects can float above cooled superconductors, avoiding contact and friction with surfaces. These possibilities pave the way for significant innovations in various fields of technology and science³³.

Additionally, there's a critical point where \mathbf{H} exceeds a certain threshold. Beyond this threshold, the material can no longer perfectly cancel the applied magnetic field, leading to the breakdown of superconductivity. In other words, with the increase of \mathbf{H} , after a limit, the material loses its superconductivity and returns to a normal conductive state. This limit can be explained via a quantum formulation in terms of Cooper pairs, which will be discussed in the further section.

B. Quantum Formulation

In 1951, F. London proposed that the magnetic flux trapped within a superconducting ring is quantized³⁴. This quantization is only observed in multiply connected geometries, such as superconducting rings^{35,36}. While the London equations provide a successful phenomenological description of zero resistance and the Meissner effect, they are ultimately classical and cannot explain all aspects of superconductivity. The first direct evidence of a macroscopic quantum phenomenon in superconductors came from experiments on superconducting rings, which behave identically in this regard regardless of being Type I or Type II. In 1961, two groups independently - B. S. Deaver and W. M. Fairbank³⁵, and R. Doll and M. Näbauer³⁶ - performed a landmark experiment based on a proposal by F. London³⁴. They cooled a tiny superconducting ring below its transition temperature while it was threaded by an external magnetic field. When this external field was subsequently removed, a current was induced in the ring to preserve the internal magnetic flux. Because the ring has zero resistance, this current flows indefinitely without dissipation and is known as a **persistent current**.

The crucial discovery was that the magnetic flux (Φ) trapped by this persistent current was not continuous but was instead quantized, only taking on integer multiples of a fundamental value, the magnetic flux quantum ($\Phi_0 = h/2e$). This observation provided the first clear justification for why a quantum description is necessary. The quantization of a macroscopic variable like magnetic flux is a direct consequence of the underlying quantum mechanics of the superconducting state. The charge carriers (Cooper pairs) are described by a single, macroscopic quantum wave function that possesses a phase. For this wave function to be physically realistic and single-valued, its phase must return to itself plus an integer multiple of 2π after one complete loop around the ring. This requirement on the phase directly imposes the condition that the magnetic flux contained within the ring must be quantized, linking a macroscopic observable to a quantum mechanical principle.

1. Supercurrent Equation

The quantum description of superconductivity begins with the formulation of a supercurrent, which requires a description of the superconducting charge carriers. The phenomenon arises from the formation of **Cooper pairs** — bound states of two electrons with opposite momenta and spins — which behave as bosonic quasiparticles³⁷. While the microscopic pairing mechanism may vary, the essential feature is that these pairs, being bosons, condense into a single, coherent macroscopic quantum state.

To phenomenologically describe this collective state, Ginzburg and Landau introduced a **complex order parameter**, $\Psi(\mathbf{r})$, often called a macroscopic wave function³⁸. Instead of describing a single particle, $\Psi(\mathbf{r})$ describes the entire condensate of Cooper pairs as a single entity.

Because $\Psi(\mathbf{r})$ represents a coherent state of quantum par-

ticles in the condensate, it obeys a Schrödinger-like equation, known as the Ginzburg-Landau equation. In this framework, the charge and mass are not those of a single electron, but the effective charge $q^* = 2e$ and mass $m^* = 2m_e$ of a Cooper pair³⁹. This treatment of a macroscopic system using a single wave function is possible because Bose-Einstein statistics allow all Cooper pairs to occupy the same quantum ground state, enforcing the system-wide phase coherence that is characteristic of superconductivity³⁰.

Delving deeper into this formalism, the order parameter has its squared modulus proportional to the local Cooper pair density. Since each Cooper pair consists of two fermions, the density of Cooper pairs $n_s = N/V$, where N is the total number of Cooper pairs and V is the volume of the superconductor, is half the density of superconducting electrons. Therefore, the squared modulus of the order parameter satisfies³⁸:

$$|\Psi(\mathbf{r})|^2 = n_s. \quad (15)$$

The current associated with the superconducting state arises from the coupling of the Cooper pair condensate to the electromagnetic field. In the presence of a magnetic vector potential \mathbf{A} , the canonical momentum operator acting on the condensate is given by:

$$\hat{\mathbf{p}}_M = -i\hbar\nabla - \frac{2e}{c}\mathbf{A}, \quad (16)$$

where $2e$ is the charge of a Cooper pair. The supercurrent density \mathbf{J} is then expressed as:

$$\mathbf{J} = \frac{2e}{2m} \left[\Psi^* \left(\frac{\hbar}{i}\nabla - \frac{2e}{c}\mathbf{A} \right) \Psi + \text{h.c.} \right], \quad (17)$$

where $2m$ is the effective mass of the Cooper pair, and “h.c.” denotes the Hermitian conjugate.

Under conditions where the spatial variation of the condensate density is negligible — i.e., in the absence of significant external perturbations or near the center of the superconducting phase — the order parameter can be approximated as:

$$\Psi(\mathbf{r}) \approx \sqrt{n_s} e^{i\theta(\mathbf{r})}, \quad (18)$$

where $\theta(\mathbf{r})$ is the local phase of the condensate. This macroscopic phase, $\theta(\mathbf{r})$, is the single most important degree of freedom for describing superconducting quantum circuits. As will be detailed in Sec. III, a difference in this phase across a tunnel junction gives rise to the **Josephson effect**, which is the fundamental principle enabling the creation of superconducting qubits. Substituting Eq. (18) into Eq. (17) yields the supercurrent density:

$$\mathbf{J} = -\frac{\mathbf{A}}{\Lambda_s c} + \frac{\hbar}{2e\Lambda_s} \nabla\theta, \quad (19)$$

$$\Lambda_s = \frac{4\pi\lambda^2}{c^2} = \frac{2m}{n_s(2e)^2} = \frac{m}{2n_s e^2}, \quad (20)$$

where λ is the London penetration depth, and the factors $2e$ and $2m$ explicitly account for the charge and mass of

Cooper pairs, respectively. This expression connects the supercurrent to the phase of the order parameter and explains the phenomenon of flux quantization: Integrating Eq. 19 over a closed loop inside the ring material yields $\oint \nabla \theta \cdot d\mathbf{l} = (2e/\hbar) \oint \mathbf{A} \cdot d\mathbf{l}$. Since the wave function must be single-valued, the total change in phase around the loop must be an integer multiple of 2π . This forces the magnetic flux $\Phi = \oint \mathbf{A} \cdot d\mathbf{l}$ to be quantized in units of the flux quantum, $\Phi_0 = h/2e$.

The uniformity of n_s is justified under equilibrium conditions well below the critical temperature and in the absence of strong spatial inhomogeneities. In this regime, the number of condensed pairs remains approximately constant throughout the material, leading to a constant Cooper pair density n_s .

When an external magnetic field is applied to a superconductor, this formalism explains the Meissner effect. A persistent supercurrent, described by Eq. 19, is induced at the surface of the material. This **screening current** flows such that it generates a magnetic field that exactly cancels the external field inside the superconductor, ensuring the magnetic field in the bulk remains zero. This interaction is central to the diamagnetic behavior of superconductors^{30,32}.

2. London Equations

From the quantum mechanical formulation of the supercurrent, both characteristic effects of superconductors — perfect conductivity and perfect diamagnetism — can be derived, leading to the so-called London equations.

To derive the first London equation, consider a time-independent Cooper pair density and a perturbation introduced by an external scalar electric potential $\phi(\mathbf{r})$. Under these conditions, the Schrödinger equation for the superconducting condensate, whose wave function is denoted by $\Psi(\mathbf{r}, t) = \sqrt{n_s} e^{i\theta(\mathbf{r}, t)}$, can be written as:

$$[\hat{H}_0 + e\phi(\mathbf{r})] \Psi(\mathbf{r}, t) = i\hbar \frac{\partial}{\partial t} \Psi(\mathbf{r}, t), \quad (21)$$

where \hat{H}_0 denotes the unperturbed Hamiltonian of the system, and $e\phi(\mathbf{r})$ represents the perturbation due to an applied electric potential. Substituting the wave function into Eq. (21) and isolating the temporal evolution of the phase leads to:

$$\hbar \frac{\partial \theta(\mathbf{r}, t)}{\partial t} = -[E_0 + e\phi(\mathbf{r})], \quad (22)$$

where E_0 is the unperturbed energy eigenvalue, independent of position.

Differentiating the supercurrent expression (Eq. 19 with respect to time, yields:

$$\frac{\partial \mathbf{J}}{\partial t} = -\frac{1}{\Lambda_s c} \frac{\partial \mathbf{A}}{\partial t} + \frac{\hbar}{e \Lambda_s} \nabla \frac{\partial \theta}{\partial t}. \quad (23)$$

Using the phase evolution relation:

$$\frac{\partial \mathbf{J}}{\partial t} = -\frac{1}{\Lambda_s c} \frac{\partial \mathbf{A}}{\partial t} - \frac{1}{\Lambda_s} \nabla \phi(\mathbf{r}). \quad (24)$$

Recognizing the electric field as:

$$\mathbf{E} = -\frac{1}{c} \frac{\partial \mathbf{A}}{\partial t} - \nabla \phi(\mathbf{r}), \quad (25)$$

the relation becomes:

$$\mathbf{E} = \Lambda_s \frac{\partial \mathbf{J}}{\partial t}, \quad (26)$$

which constitutes the **first London equation**, capturing the ideal conductivity of superconductors. This equation implies that an electric field induces a proportional change in the supercurrent density, with the proportionality governed by Λ_s , a material-specific parameter.

Two main implications follow:

- An applied electric field leads to a continuous acceleration of the supercurrent, in stark contrast to normal resistive behavior. This illustrates the phenomenon of zero electrical resistance in superconductors.
- The evolution of the supercurrent is directly determined by the local electric field, establishing a dynamic response rather than a dissipative one.

To derive the **second London equation**, which characterizes perfect diamagnetism, consider the curl of the supercurrent expression:

$$\nabla \times \mathbf{J} = -\frac{1}{\Lambda_s c} \nabla \times \mathbf{A} + \frac{\hbar}{e \Lambda_s} \nabla \times \nabla \theta. \quad (27)$$

Since the curl of a gradient vanishes,

$$\nabla \times \mathbf{J} = -\frac{1}{\Lambda_s c} \mathbf{B}. \quad (28)$$

Taking the curl of both sides and using Ampère's Law, Eq. (5), it yields:

$$\nabla \times \left(\frac{c}{4\pi} \nabla \times \mathbf{B} \right) = -\frac{1}{\Lambda_s c} \mathbf{B}. \quad (29)$$

Using the vector identity $\nabla \times (\nabla \times \mathbf{B}) = \nabla(\nabla \cdot \mathbf{B}) - \nabla^2 \mathbf{B}$ and Gauss' law for magnetism $\nabla \cdot \mathbf{B} = 0$, the expression reduces to:

$$-\frac{c}{4\pi} \nabla^2 \mathbf{B} = -\frac{1}{\Lambda_s c} \mathbf{B}. \quad (30)$$

Rearranging, and defining the *London penetration depth* λ as in Eq. (20), one obtains:

$$\nabla^2 \mathbf{B} = \frac{1}{\lambda^2} \mathbf{B}. \quad (31)$$

The second London equation describes how magnetic fields decay exponentially inside a superconductor, a direct manifestation of the Meissner effect. This result confirms that superconductors exhibit perfect diamagnetism by completely expelling magnetic fields from their interior (except within a thin surface layer of thickness λ).

The second London equation, $\nabla^2 \mathbf{B} = \mathbf{B}/\lambda^2$, has a straightforward physical interpretation. For a simple geometry, such as a magnetic field parallel to the surface of a semi-infinite superconductor, its solution shows that the field decays exponentially from the surface into the bulk: $B(x) = B(0)e^{-x/\lambda}$. The parameter λ is therefore the characteristic length scale over which an external magnetic field is screened. This depth is a crucial material property. In conventional superconductors used for quantum circuits, like aluminum and niobium, λ is typically in the range of 50–100 nm³². For high-temperature cuprate superconductors such as YBa₂Cu₃O_{7- δ} , the penetration depth can be larger, often exceeding 200 nm⁴⁰.

This short-scale magnetic screening is fundamental to modern quantum technologies. It allows for the fabrication of superconducting films where, **even though the film thickness (typically 50–100 nm) is comparable to the London penetration depth, the screening effect is critical for confining electromagnetic fields and creating high-quality-factor resonators.** This property is heavily exploited in the design of superconducting qubits and resonators, **contributing to the low-noise electromagnetic environment necessary for achieving high coherence**⁴¹. However, achieving high coherence ultimately depends on a combination of many factors, including the mitigation of TLS defects, the Purcell effect, packaging, and quasiparticle density, **not solely on the Meissner effect**^{7,8,22}.

Together, the London equations—derived from the quantum treatment of the superconducting condensate—encapsulate the two defining properties of superconductors: zero electrical resistance and perfect diamagnetism. They describe how a superconductor responds to external magnetic fields by generating surface currents that exactly cancel the interior field, leading to the magnetic field’s expulsion.

III. JOSEPHSON EFFECT

The Josephson effect, discovered by physicist Brian D. Josephson⁴² in the early 1960s, involves the phase-dependent behavior of electric currents in superconductors. Afterward, Philip W. Anderson recognized the significance of Josephson’s work, exploring the theoretical concepts behind the effect^{43,44}. This discovery has fundamental implications for quantum coherence in macroscopic systems and has practical applications in fields such as metrology and superconducting electronics.

The Josephson effect arises from the quantum mechanical tunneling of Cooper pairs across a weak coupling interface—termed a *Josephson junction*—connecting two bulk superconductors²⁰. A Josephson junction is fundamentally characterized by a non-superconducting region (the “weak link”) that permits phase-coherent coupling of the superconducting order parameters. This weak link may manifest as: (i) an insulating barrier, enabling tunneling through a classically forbidden region; (ii) a normal metal layer, rendered superconducting via the proximity effect through Andreev reflection processes; or (iii) a geometrically constrained region (e.g., a nanoscale constriction) within an otherwise homogeneous superconducting medium³⁰. Examples of these configurations

can be visualized in Fig. 3.

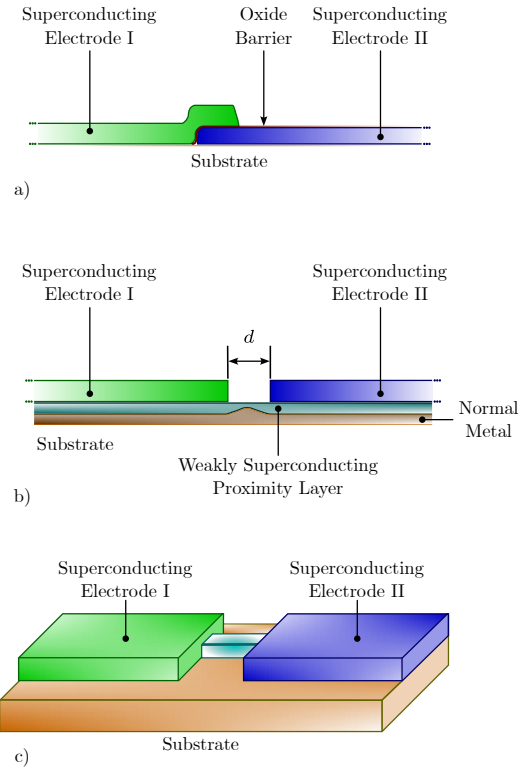


FIG. 3. Three types of Josephson junction: a) Superconductor-Insulator-Superconductor; b) Superconductor-Normal Metal-Superconductor; c) Superconductor-Constriction-Superconductor³⁰.

The junction’s defining property—its critical current-phase relation—emerges from the interplay between gauge symmetry breaking and macroscopic quantum coherence, establishing it as a cornerstone of superconducting quantum electronics.

A. DC Josephson Effect

A basic quantitative formulation of the Josephson effect begins with the assumption of two superconductors, labeled A and B, weakly coupled through a thin insulating barrier C. This configuration results in a potential barrier that is classically forbidden for Cooper pairs, making their transfer across the junction possible only via quantum tunneling.

Assuming that both superconductors A and B have well-defined numbers of Cooper pairs, denoted by N_A and N_B respectively, each superconductor can be described by its corresponding Fock state $|N_A\rangle$ and $|N_B\rangle$. These are eigenstates of the respective number operators, and, **for small superconducting islands where charging effects are significant, can also be treated as approximate eigenstates of the unperturbed Hamiltonians of each isolated superconductor.** The total quantum

state of the coupled system is then given by:

$$|\Psi\rangle = |N_A\rangle \otimes |N_B\rangle \equiv |N_A, N_B\rangle. \quad (32)$$

If the tunneling of m Cooper pairs from A to B is considered (such that the total number of particles remains conserved), the resulting state becomes:

$$|m\rangle = |N_A - m, N_B + m\rangle. \quad (33)$$

This framework models tunneling as a coherent process that changes the particle number in each superconductor symmetrically. States of the form $|m\rangle$ form a complete basis for the Hilbert space of the junction.

The tunneling process can then be described by a Hamiltonian of the form:

$$\hat{H}_T = -\frac{1}{2}E_J \sum_m [|m\rangle\langle m+1| + |m+1\rangle\langle m|], \quad (34)$$

where E_J is the Josephson energy, associated with the tunneling of a single Cooper pair across the junction. Higher-order terms of the form $|m\rangle\langle m+n|$ with $n > 1$ are neglected under the assumption that the tunneling is weak, making multiple simultaneous pair transitions highly improbable and their contributions exponentially suppressed. This justifies a nearest-neighbor coupling model.

To diagonalize \hat{H}_T , consider its analogy with a one-dimensional tight-binding Hamiltonian with hopping amplitude $-E_J/2$ and lattice spacing 1. The eigenstates of such a Hamiltonian are delocalized Bloch-like states defined by:

$$|\theta\rangle = \sum_{m=-\infty}^{\infty} e^{im\theta} |m\rangle, \quad (35)$$

where $\theta \in [0, 2\pi)$ is the conjugate variable to m , interpreted as a phase. The inverse transformation is given by:

$$|m\rangle = \frac{1}{2\pi} \int_0^{2\pi} e^{-im\theta} |\theta\rangle d\theta. \quad (36)$$

In this basis, the tunneling Hamiltonian becomes diagonal:

$$\hat{H}_T = -E_J \cos \hat{\theta}, \quad (37)$$

where the operator $e^{i\hat{\theta}}$ is defined by:

$$e^{i\hat{\theta}} = \frac{1}{2\pi} \int_0^{2\pi} e^{i\theta} |\theta\rangle\langle\theta| d\theta. \quad (38)$$

At this point, it is essential to provide a physical interpretation of the phase variable θ . While the θ appearing in the phase basis $|\theta\rangle$ is a mathematical construct arising from the Fourier transform of number states $|m\rangle$, it gains physical relevance when related to the macroscopic quantum phase difference across the Josephson junction. This identification becomes meaningful when the superconducting phase is introduced via the Ginzburg-Landau theory.

Connection to Superconducting Phase and Magnetic Flux

Recalling the macroscopic phase θ of the order parameter introduced in Eq. (18), the essential physics of a Josephson junction emerges when a weak link connects two superconductors. When two superconductors A and B are connected, the difference in their macroscopic phases, φ , acquires physical significance. More formally, the **gauge-invariant phase difference** is given by³⁰:

$$\varphi = (\theta_A - \theta_B) - \frac{2e}{\hbar} \int \mathbf{A} \cdot d\mathbf{l}, \quad (39)$$

where θ_A and θ_B are the respective macroscopic phases, \mathbf{A} is the magnetic vector potential, and the integral is a line integral along a path $d\mathbf{l}$ across the junction.

We now simplify this by assuming the absence of any external magnetic field threading the junction area. Although the supercurrent itself generates a magnetic field and thus a vector potential \mathbf{A} , a gauge can often be chosen such that \mathbf{A} is parallel to the current flow (along the superconductor surfaces). Since the integration path $d\mathbf{l}$ across the junction barrier is typically perpendicular to this current flow, the dot product $\mathbf{A} \cdot d\mathbf{l}$ becomes negligible. Under these common assumptions, the gauge-invariant phase difference effectively reduces to the difference between the macroscopic phases:

$$\varphi \approx \theta_A - \theta_B. \quad (40)$$

Given this perspective, the *reduced magnetic flux* φ , the *magnetic flux* ϕ , and the *reduced flux quantum* ϕ_0 are defined by:

$$\varphi \equiv \frac{\phi}{\phi_0} \pmod{2\pi}, \quad \phi_0 = \frac{\hbar}{2e}. \quad (41)$$

This identification justifies interpreting the operator $\hat{\theta}$ as representing the phase difference across the junction and establishes φ as its physically relevant counterpart. Therefore, the tunneling Hamiltonian can be rewritten in terms of the reduced flux:

$$\hat{H}_T = -E_J \cos \hat{\varphi}. \quad (42)$$

where $\hat{\varphi}$ denotes the quantum operator associated with the gauge-invariant phase difference across the junction. Within the canonical quantization framework, $\hat{\varphi}$ and the number operator \hat{n} , which accounts for the net Cooper pair transfer across the junction, satisfy the commutation relation¹¹

$$[\hat{\varphi}, \hat{n}] = i, \quad (43)$$

analogous to the canonical position-momentum relation in quantum mechanics. This conjugate structure imposes a fundamental quantum uncertainty between phase and charge, precluding their simultaneous precise determination.

Derivation of the DC Josephson Relation

To derive the expression for the supercurrent, consider a wave packet in the phase basis, written as:

$$|\psi\rangle = \sum_{\varphi} \mu_{\varphi} |\varphi\rangle, \quad (44)$$

where μ_{φ} are complex amplitudes over the continuous phase variable φ . The group velocity of this wave packet is given by the derivative of the energy expectation value with respect to its conjugate variable, φ . This relationship is a quantum-mechanical extension of Hamilton's equations, where the current (proportional to velocity) is given by the derivative of the energy (the Hamiltonian) with respect to the conjugate momentum (the phase). The supercurrent is the flow of charge across the junction, which corresponds to the rate of change of the number of transferred Cooper pairs. We define the supercurrent I_s in terms of the time derivative of the expectation value of the number operator, \hat{n} :

$$I_s = 2e \frac{d\langle \hat{n} \rangle}{dt}. \quad (45)$$

Using Ehrenfest's theorem, the evolution of the expectation value is given by the commutator with the Hamiltonian:

$$\frac{d\langle \hat{n} \rangle}{dt} = \frac{1}{i\hbar} \langle [\hat{n}, \hat{H}_T] \rangle, \quad (46)$$

where the tunneling Hamiltonian is given by Eq. (42). The commutator can be evaluated using the canonical commutation relation given by Eq. (43). For any analytic function $f(\hat{\varphi})$, this implies the general relation $[\hat{n}, f(\hat{\varphi})] = -i \frac{\partial f}{\partial \hat{\varphi}}$ ⁴⁵. Applying this rule to our Hamiltonian gives:

$$[\hat{n}, \hat{H}_T] = -i \frac{\partial}{\partial \hat{\varphi}} (-E_J \cos(\hat{\varphi})) = -i E_J \sin(\hat{\varphi}). \quad (47)$$

Substituting this back into the equation for the time evolution yields:

$$\frac{d\langle \hat{n} \rangle}{dt} = \frac{1}{i\hbar} \langle -i E_J \sin(\hat{\varphi}) \rangle = \frac{E_J}{\hbar} \langle \sin(\hat{\varphi}) \rangle. \quad (48)$$

This leads directly to the expression for the supercurrent:

$$I_s = 2e \left(\frac{E_J}{\hbar} \right) \langle \sin(\hat{\varphi}) \rangle. \quad (49)$$

In the semiclassical limit, where the phase is a well-defined quantity, we can approximate $\langle \sin(\hat{\varphi}) \rangle \approx \sin(\langle \hat{\varphi} \rangle)$. This gives the celebrated **DC Josephson relation**:

$$I_s = I_c \sin(\varphi), \quad (50)$$

where $\varphi = \langle \hat{\varphi} \rangle$ is the expectation value of the phase difference and the critical current I_c is defined as:

$$I_c = \frac{2eE_J}{\hbar}. \quad (51)$$

Physical Interpretation

The DC Josephson relation, Eq. (50), encapsulates two key features of coherent charge transport in Josephson junctions:

- A non-zero supercurrent can flow across the junction even in the absence of an applied voltage, provided there exists a finite phase difference φ between the superconducting leads;
- The maximum achievable supercurrent is given by the critical current I_c , beyond which the junction enters a dissipative regime.

Importantly, Eq. (50) is valid in the semiclassical regime, where the phase difference is well-defined and quantum fluctuations are negligible. It does *not* require the system to be in an eigenstate of the tunneling Hamiltonian \hat{H}_T . In fact, the energy eigenstates of \hat{H}_T are delocalized in phase space and exhibit a vanishing expectation value of the current operator due to symmetry. The DC Josephson relation describes the current in coherent or semiclassical states, characterized by a narrow distribution in phase.

The Josephson effect thus exemplifies macroscopic quantum coherence, manifesting as a non-dissipative current determined solely by the phase difference. This phenomenon underpins the operation of superconducting quantum circuits and serves as a cornerstone in the architecture of superconducting qubits.

B. AC Josephson Effect

The application of a static voltage V across a Josephson junction induces coherent temporal dynamics in the superconducting phase difference. This behavior arises from the fundamental conjugate relation between the superconducting phase operator $\hat{\varphi}$ and the number operator \hat{n} , given by Eq. 43. When a constant voltage is applied, the Hamiltonian describing the junction becomes:

$$\hat{H} = -E_J \cos \hat{\varphi} - 2eV \hat{n}, \quad (52)$$

where the second term accounts for the potential energy associated with the transfer of Cooper pairs across the voltage bias.

To determine the resulting phase dynamics, consider the Heisenberg equation of motion for $\hat{\varphi}(t)$:

$$\frac{d\hat{\varphi}}{dt} = \frac{i}{\hbar} [\hat{H}, \hat{\varphi}] = \frac{2e}{\hbar} V. \quad (53)$$

This yields a linear time evolution for the operator:

$$\hat{\varphi}(t) = \hat{\varphi}_0 + \frac{2eV}{\hbar} t. \quad (54)$$

To obtain a measurable quantity, one considers the expectation value of the phase operator in a semiclassical state where

quantum fluctuations are negligible. Denoting the expectation value by $\varphi(t) = \langle \hat{\phi}(t) \rangle$, it follows that:

$$\frac{d\varphi}{dt} = \frac{2e}{\hbar} V, \quad (55)$$

which defines the **AC Josephson relation**.

Integrating Eq. (55), the phase difference evolves as:

$$\varphi(t) = \varphi_0 + \omega_J t, \quad (56)$$

where $\omega_J = 2eV/\hbar$ is the *Josephson frequency* associated with the applied voltage.

Substituting this time-dependent phase into the first Josephson relation yields the supercurrent:

$$I_s(t) = I_c \sin \varphi(t) = I_c \sin(\varphi_0 + \omega_J t). \quad (57)$$

The following conclusions emerge from this analysis:

- A constant voltage bias across the junction results in an alternating supercurrent of amplitude I_c and frequency ω_J ;
- The Josephson junction functions as a voltage-to-frequency converter, with a conversion factor $f_J = (2e/h)V$;
- The AC Josephson effect forms the physical basis for high-precision voltage standards in quantum metrology.

This phenomenon exemplifies macroscopic quantum coherence, linking phase dynamics and electrical transport in a fundamentally quantum mechanical manner. It also underpins the operation of superconducting devices at microwave and radio frequencies, enabling technologies ranging from quantum voltage standards to superconducting qubits.

IV. CIRCUIT QUANTUM ELECTRODYNAMICS

The preceding sections have comprehensively covered the foundational aspects of superconductivity, ranging from classical formulations to the quantum phenomena known as the Josephson effect. Building upon this groundwork, the forthcoming segment delves into Circuit Quantum Electrodynamics (cQED)⁷, marking a transition from theoretical underpinnings to practical applications in the realm of electrical circuits and quantum mechanics. In this section, the focus shifts towards an in-depth exploration of different devices within the context of cQED such as resonators and transmons.

A. Microwave Resonators

Microwave resonators, pivotal components in quantum circuits, exhibit intricate interactions with microwave photons reminiscent of those between atoms and light in cavity quantum electrodynamics⁴⁶. The upcoming section initially navigates through resonators classically, likening their behavior to classical oscillatory systems and electromagnetic waves.

Transitioning to a quantum perspective, it delves into the interaction of quantized electromagnetic fields with matter, elucidating resonators' unique quantum phenomena. This exploration extends to resonators' integration into transmission line architectures, elucidating their pivotal role in coherent quantum information manipulation and transmission.

1. Classical Resonator

To understand the classical behavior of a resonator, consider an LC circuit composed of an inductor with inductance L and a capacitor with capacitance C arranged in parallel. This configuration is illustrated in Fig. 4.

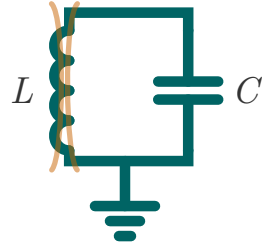


FIG. 4. Schematic representation of a classical LC resonator. The inductance L and capacitance C are arranged in parallel, forming an idealized resonant circuit.

Assign a time-dependent voltage $V(t)$ and flux $\phi(t)$ to the top node of the resonator, with a current $I(t)$ flowing in the counter-clockwise direction. In the absence of dissipation, the total energy in the system is stored alternately in the electric field of the capacitor and the magnetic field of the inductor.

Using Kirchhoff's laws, the dynamics of the LC circuit can be described by a second-order differential equation. This is the equation of a harmonic oscillator, whose natural angular frequency is given by:

$$\omega_r = \frac{1}{\sqrt{LC}}. \quad (58)$$

The general solutions for the time evolution of current and voltage in the circuit are:

$$I(t) = I_0 \cos(\omega_r t + \vartheta), \quad (59)$$

$$V(t) = L \frac{dI}{dt} = -L\omega_r I_0 \sin(\omega_r t + \vartheta), \quad (60)$$

where I_0 is the amplitude of the oscillating current, $V_0 = L\omega_r I_0$ is the amplitude of the voltage, and ϑ is the initial phase, determined by the initial conditions of the system.

The *characteristic impedance* of the resonator is defined as the ratio between the voltage and current amplitudes:

$$Z_r = \frac{V_0}{I_0} = \sqrt{\frac{L}{C}}. \quad (61)$$

This impedance plays a central role in the coupling of the resonator to external circuits and to quantum systems, as will be discussed in subsequent sections.

In addition, the quality factor \mathcal{Q} , which is the ratio of its resonant frequency ω_r to its decay rate κ , quantifies the resonator's energy retention capacity by comparing the time-averaged stored energy to the energy dissipated per oscillation cycle. In practical systems **not in a superconducting state**, dissipation arises from resistive losses, introducing a decay rate. This modifies the ideal harmonic oscillator equation to a damped form, governing the exponential decay of oscillations. For a parallel RLC configuration, \mathcal{Q} is directly proportional to the resistance R and inversely proportional to the characteristic impedance Z_r . (For comparison, in a series RLC configuration, the lossless limit corresponds to $R \rightarrow 0$, whereas for a parallel RLC it is $R \rightarrow \infty$.)

The idealized lossless resonator ($R \rightarrow \infty$ for a parallel RLC) corresponds to $\mathcal{Q} \rightarrow \infty$, reflecting perpetual energy exchange. In quantum-electrodynamic applications, high \mathcal{Q} -values ($\mathcal{Q} \gg 1$) are critical for minimizing photon loss and decoherence, as they ensure long-lived electromagnetic field confinement.

This classical resonator model provides the foundation for understanding superconducting resonators and their role in the cQED architecture used in superconducting qubits.

2. Quantum Resonator – Simple Formulation

The quantum formulation of the resonator highlights the transition from classical to quantum descriptions, emphasizing the scales at which quantum effects become significant. While classical physics dominates at macroscopic scales, the focus shifts to systems where quantum mechanics reveals its granularity. By quantizing flux and charge variables through employing **canonical** quantization techniques, it is possible to construct the Hamiltonian operator to accurately capture the resonator's quantum behavior. **Thus**, the exploration of zero-point energy and Gaussian probability distributions further elucidates the quantum nature of the system, providing insights into fundamental phenomena.

Within this perspective, a quantum formulation is built to approach the resonator. We start with the *classical Hamiltonian* H of the parallel LC circuit:

$$H = \frac{Q^2}{2C} + \frac{1}{2}C\omega_r^2\phi^2, \quad (62)$$

where Q is the charge on the capacitor, ϕ is the flux through the inductor, and $\omega_r = 1/\sqrt{LC}$ is the resonant frequency of the circuit.

In this formulation, the classical Hamiltonian H for the parallel LC circuit mirrors the form of the Hamiltonian for a harmonic oscillator, which is depicted in Appendix A, Eq. (A1). The parallel between the two systems becomes evident when comparing their respective energy expressions. In the case of the LC circuit, H consists of the sum of kinetic and potential energy terms, akin to the expression for a harmonic oscillator. Specifically, the first term corresponds to the kinetic energy term, while the second term represents the potential energy term. This parallel underscores the resonator's behavior akin

to that of a harmonic oscillator, albeit in the context of electrical circuits.

Using Hamilton's equations of motion, it is possible to verify that the flux and the charge variables constitute a pair of canonical conjugated variables, where they play the role of generalized position and generalized momentum, respectively. This verification is seen below:

$$\frac{\partial H}{\partial \phi} = C\omega_r^2\phi = -\frac{dQ}{dt} = -I, \quad (63)$$

$$\frac{\partial H}{\partial Q} = \frac{Q}{C} = V = \frac{d\phi}{dt}. \quad (64)$$

The transition to the quantum description is made via canonical quantization. The classical Poisson bracket for these conjugate variables is $\{\phi, Q\}_{\text{PB}} = 1$. This is replaced by the quantum commutator according to the rule $\{\cdot, \cdot\}_{\text{PB}} \rightarrow \frac{1}{i\hbar}[\cdot, \cdot]$. This promotes the classical variables ϕ and Q to the **flux operator** $\hat{\phi}$ and the **charge operator** \hat{Q} , which must obey the canonical commutation relation:

$$[\hat{\phi}, \hat{Q}] = i\hbar, \quad (65)$$

and we define the dimensionless operators $\tilde{\phi}$ and \tilde{Q} :

$$\tilde{\phi} = \sqrt{\frac{C\omega_r}{2\hbar}}\hat{\phi}, \quad (66)$$

$$\tilde{Q} = \sqrt{\frac{1}{2\hbar C\omega_r}}\hat{Q}, \quad (67)$$

with the commutation relation:

$$[\tilde{\phi}, \tilde{Q}] = \frac{i}{2}. \quad (68)$$

Given that, the Hamiltonian for the resonator becomes:

$$\hat{H} = \hbar\omega_r(\tilde{Q}^2 + \tilde{\phi}^2), \quad (69)$$

manipulating Eq. (69), it can be rewritten as:

$$\hat{H} = \hbar\omega_r \left[(\tilde{\phi} - i\tilde{Q})(\tilde{\phi} + i\tilde{Q}) + \frac{1}{2} \right]. \quad (70)$$

Relating Eq. (70) with the *annihilation and creation operators* \hat{a} and \hat{a}^\dagger , respectively, the following relations can be derived:

$$\begin{cases} \hat{a} &= \tilde{\phi} + i\tilde{Q} \\ \hat{a}^\dagger &= \tilde{\phi} - i\tilde{Q} \end{cases}, \quad (71)$$

$$\hat{\phi} = \sqrt{\frac{\hbar}{2C\omega_r}}(\hat{a}^\dagger + \hat{a}), \quad (72)$$

$$\hat{Q} = i\sqrt{\frac{\hbar C\omega_r}{2}}(\hat{a}^\dagger - \hat{a}), \quad (73)$$

$$\hat{H} = \hbar\omega_r \left(\hat{a}^\dagger \hat{a} + \frac{1}{2} \right), \quad (74)$$

where the commutation relation between \hat{a}^\dagger and \hat{a} can be seen in Eq. (A4).

Additionally, some useful relations can also be derived within the zero point energy, where ϕ_{zpf} represents the *zero-point fluctuation of the flux variable* in the resonator, and Q_{zpf} represents the *zero-point fluctuation of the charge variable* in the resonator. These terms refer to the values that characterize the minimum fluctuation or uncertainty in the flux and charge variable due to the Heisenberg uncertainty principle, respectively:

$$\langle \tilde{\phi} \rangle = \langle \tilde{Q} \rangle = 0, \quad (75)$$

$$\langle \tilde{\phi}^2 \rangle = \phi_{zpf}^2 = \frac{\hbar}{2C\omega_r}, \quad (76)$$

$$\langle \tilde{Q}^2 \rangle = Q_{zpf}^2 = \frac{\hbar C\omega_r}{2}. \quad (77)$$

Moreover, it is conceived an analogy to the mechanical variables in a Harmonic Quantum Oscillator. Defining $|\phi\rangle$ and $|q\rangle$ eigenstates of flux and charge:

$$\langle \phi' | \hat{\phi} | \phi \rangle = \phi \delta(\phi' - \phi), \quad (78)$$

$$\langle \phi' | \hat{Q} | \phi \rangle = -i\hbar \delta(\phi' - \phi) \nabla. \quad (79)$$

Projecting the zero point energy eigenstates on the respective eigenstates:

$$\langle \phi | 0 \rangle = \frac{1}{\phi_{zpf}} \frac{1}{\sqrt{2\pi}} \exp \left(-\frac{\phi^2}{2\phi_{zpf}^2} \right), \quad (80)$$

$$\langle q | 0 \rangle = \frac{1}{Q_{zpf}} \frac{1}{\sqrt{2\pi}} \exp \left(-\frac{q^2}{2Q_{zpf}^2} \right). \quad (81)$$

Following the quantum formulation built until now, it is clear that the energy eigenstates $|n\rangle$ are stationary, meaning the expectation values $\langle \hat{\phi} \rangle$ and $\langle \hat{Q} \rangle$ are zero and do not evolve in time. To observe dynamics that resemble a classical oscillator, one must consider a superposition of these eigenstates. A *coherent state* $|z\rangle$ is a specific superposition that achieves this, where the expectation values of the flux and charge operators, $\langle \hat{\phi}(t) \rangle$ and $\langle \hat{Q}(t) \rangle$, oscillate sinusoidally in time. This behavior stems from the nature of coherent states in quantum mechanics (as described in Appendix A).

Coherent states are defined as the eigenstates of the non-Hermitian annihilation operator \hat{a} , satisfying $\hat{a}|z\rangle = z|z\rangle$. They mimic the classical oscillations with a well-defined phase and amplitude. Thus, this state presents average values of the quadrature operators (which represent the canonical conjugate observables associated with phase space) corresponding to the classical amplitudes, while the standard deviations of these

quadratures are determined by the zero-point fluctuation values of the ground state:

$$|z\rangle = e^{-\frac{|z|^2}{2}} \sum_{n=0}^{\infty} \frac{z^n}{\sqrt{n!}} |n\rangle. \quad (82)$$

The time evolution of such a state is so that its *eigenvalue* z gains a phase factor:

$$|z(t)\rangle = |z(0)e^{-i\omega_r t}\rangle, \quad (83)$$

where the average values of flux and charge are given as functions of time by:

$$\langle \phi(t) \rangle = \phi_{zpf} \langle z(t) | (\hat{a}^\dagger + \hat{a}) | z(t) \rangle = 2\phi_{zpf} \Re \{ e^{-i\omega_r t} z(0) \}, \quad (84a)$$

$$\langle \phi(t) \rangle = 2\phi_{zpf} |z(0)| \cos(\omega_r t + \xi), \quad (84b)$$

$$\langle Q(t) \rangle = iQ_{zpf} \langle z(t) | (\hat{a}^\dagger - \hat{a}) | z(t) \rangle = 2Q_{zpf} \Im \{ e^{-i\omega_r t} z(0) \}, \quad (84c)$$

$$\langle Q(t) \rangle = 2Q_{zpf} |z(0)| \sin(\omega_r t + \xi), \quad (84d)$$

where $\xi \equiv \arg z(0)$ is the phase of $z(0)$.

From the analysis of the quantum formulation of the resonator, it is possible to verify that the probability amplitudes for the flux and charge variables follow Gaussian distributions for the ground state, being normalized to represent a quantum zero-point energy state. These distributions are normalized to ensure that they represent a quantum zero-point energy state accurately. The Gaussian nature of the probability distributions implies that the most probable values of the flux and charge variables cluster around their respective mean values, with decreasing probability as the values deviate further from the mean. This behavior is characteristic of systems in equilibrium.

In practice, the relevance of the quantization procedure for LC oscillators hinges on two critical conditions. First, the oscillator must be effectively isolated from uncontrollable factors to keep its energy levels much narrower than their spacing. This requires a high-quality factor \mathcal{Q} for the oscillator. Superconductors like aluminum and niobium, because of their low losses, are suitable for achieving the necessary \mathcal{Q} values. The second condition is that the energy gap between adjacent quantum states should exceed thermal energy. Microwave frequency circuits, operated at low temperatures (around 10 mK) in dilution refrigerators, satisfy this condition. With these requirements met, a microwave-range oscillator can operate in the quantum regime. It can be prepared in its ground state $|n=0\rangle$ by allowing it to evolve for a few photon lifetimes⁷.

3. Quantum Resonator – Transmission Line

Understanding the properties of transmission line resonators within the context of cQED is important for optimizing their performance in several applications, such as the exploration of synergistic effects when coupled to other superconducting elements, such as qubits. These interactions can

lead to novel phenomena and effects that are not present in isolation. In addition, integrating the discussion of transmission line resonators into the cQED framework facilitates experimental validation of theoretical predictions and opens up possibilities for exploring new regimes of operation in quantum technologies.

In this section, the significance of multimode structures is explored by examining the electromagnetic properties of coplanar waveguide resonators, which are modeled as linear, dispersion-free one-dimensional media.

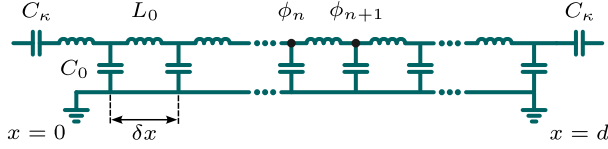


FIG. 5. Telegrapher model of an open-ended transmission line resonator of length d . L_0 and C_0 are, respectively, the inductance and capacitance associated with each node n of flux ϕ_n . The resonator is coupled to external transmission lines (not shown) at its input and output ports via the capacitors C_K .

Consider the circuit depicted in Fig. 5, composed of interleaved inductances L_n and shunt capacitances C_n . The nodes are physically distanced by δx , adding up to a total length of d . It is important to visualize that $C_0 = \delta x c_0$ and $L_0 = \delta x l_0$, with the lower case notation for *physical quantity per unit length*. By quantizing fields in transmission lines, it is determined the potential to create resonators with distributed parameters. Thus, the circuit's Hamiltonian using charge Q_n and flux ϕ_n variables:

$$H = \sum_{n=0}^{N-1} \left[\frac{1}{2C_0} Q_n^2 + \frac{1}{2L_0} (\phi_{n+1} - \phi_n)^2 \right]. \quad (85)$$

Consider the linear charge density as a function of $n\delta x$:

$$\lambda(n\delta x) = \frac{Q_n}{\delta x}. \quad (86)$$

In the limit as $\delta x \rightarrow 0$, the classical Hamiltonian can be expressed as the following integral:

$$H = \int_0^d \left(\frac{1}{2c_0} \lambda(x)^2 + \frac{1}{2l_0} (\partial_x \phi(x))^2 \right) dx. \quad (87)$$

Obtaining the equations of motion derived from Eq. (87) using Hamiltonian classical field theory:

$$\dot{\lambda} = -\frac{\delta \mathcal{H}}{\delta \phi} = -\frac{1}{l_0} \frac{\partial^2 \phi}{\partial x^2}, \quad (88)$$

$$\dot{\phi} = \frac{\delta \mathcal{H}}{\delta \lambda} = \frac{1}{c_0} \lambda. \quad (89)$$

Considering the wave propagation velocity v_0 on the circuit, whose equations lead to the flux wave equation:

$$v_0^2 \frac{\partial^2 \phi}{\partial x^2} = \frac{\partial^2 \phi}{\partial t^2}, \quad (90)$$

where:

$$v_0 = \frac{1}{\sqrt{l_0 c_0}}. \quad (91)$$

The general solution for $\phi(x, t)$ can be expressed as:

$$\phi(x, t) = \int_{-\infty}^{\infty} A_k \cos(kx + \alpha_k) \cos(\omega t + \beta_k) dk, \quad (92)$$

where A_k is the amplitude, α_k is the spatial phase constant, and β_k is the temporal phase constant for each wave component with a specific wave number k . Here, the frequency $\omega = v_0 k$. From the continuity equation, the open-circuit boundary condition is obtained at the position x_{oc} (x_{oc} represents the physical coordinates of the open ends of the transmission line resonator, such as $x = 0$ and $x = d$, where the boundary conditions are applied):

$$I(x_{oc}, t) = -\frac{1}{l_0} \frac{\partial \phi}{\partial x} \Big|_{x_{oc}} = 0, \quad (93)$$

and from the flux definition, the short-circuit boundary condition in V_{sc} is obtained:

$$V(x_{sc}, t) = \frac{\partial \phi}{\partial t} \Big|_{x_{sc}} = 0. \quad (94)$$

In the case of an open-ended half-wavelength transmission line, both ends are in an open circuit, leading to $k = \frac{n\pi}{d}$ and $\alpha_k = 0$. Similarly, for a quarter-wavelength transmission line, **one end is shorted and the other is open**, resulting in $k = (n + \frac{1}{2}) \frac{\pi}{d}$ and $\alpha_k = 0$. The constants A_k and β_k are determined by the initial conditions. Therefore, Eq. (92) can be expressed as:

$$\phi(x, t) = \sum_n A_n \cos(k_n x) \cos(\omega_n t + \beta_n). \quad (95)$$

The separation of variables requires explicit normalization of the spatial eigenfunctions $\cos(k_n x)$ to establish an orthonormal basis. While these eigenfunctions satisfy orthogonality over the resonator length d , their normalization is achieved through the introduction of a $\sqrt{2}$ prefactor, yielding the condition:

$$\int_0^d \left[\sqrt{2} \cos(k_n x) \right] \left[\sqrt{2} \cos(k_m x) \right] dx = \delta_{nm} d. \quad (96)$$

This normalization permits the flux field $\phi(x, t)$ to be expressed as a superposition of orthonormal modes. The resulting form:

$$\phi(x, t) = \sum_n \sqrt{2} A_n \cos(k_n x) (\cos(\omega_n t + \beta_n)) \quad (97)$$

explicitly separates the spatial and temporal dependencies. This decomposition naturally leads to the identification of:

- Spatial mode functions: $u_n(x) = \sqrt{2} \cos(k_n x)$
- Temporal amplitudes: $\phi_n(t) = A_n \cos(\omega_n t + \beta_n)$

establishing the foundation for canonical quantization through the product decomposition $\phi(x, t) = \sum_n u_n(x) \phi_n(t)$.

The spatial and time-dependent components are defined such that $u_n(x)$ has a length norm d for the transmission line, and $\phi_n(t)$ carries the constants set by the initial conditions. It's worth noting that $u_n(x)$ is already fully specified by the mode index n , while $\phi_n(t)$ remains a dynamical variable. Inserting $\phi(x, t)$ into the Hamiltonian (Eq. (87)) results in a summation of uncoupled harmonic oscillators:

$$H = \sum_{n=0}^{\infty} \left(\frac{1}{2} \frac{Q_n^2}{C_r} + \frac{1}{2} C_r \omega_n^2 \phi_n^2 \right). \quad (98)$$

Here, $C_r = dC_0$ represents the total capacitance of the line, $Q_n = C_r \dot{\phi}_n(t)$ is the charge conjugate to ϕ_n , and the angular frequency ω_n represents the modal frequency of the n -th standing wave mode of the transmission line resonator.

Generalizing Eqs. (72) and (73) for the operators $\hat{\phi}$ and \hat{Q} for each pair Q_n and ϕ_n in Eq. (98), the quantum Hamiltonian for a transmission line is obtained:

$$\hat{H} = \sum_{n=0}^{\infty} \hbar \omega_n \left(\hat{a}_n^\dagger \hat{a}_n + \frac{1}{2} \right), \quad (99)$$

which represents a sum of quantum harmonic oscillators, each with frequency ω_n and ladder operators \hat{a}_n and \hat{a}_n^\dagger .

From the analysis of the modeling of the transmission line, it is observed that the behavior of a transmission line can be approximated to a sum of uncoupled harmonic oscillators. This approximation is possible by ignoring the presence of the input and output port capacitors and by considering a homogeneous medium forming of the resonator.

B. Practical Examples of Microwave Resonators

In the realm of cQED, microwave resonators share fundamental principles related to electromagnetic fields, resonant behavior, and energy storage. Their specific designs and applications may differ, but their common features make them essential tools in various scientific and engineering contexts. Some practical examples can be cited:

- **Coaxial stub cavities:** A specific type of resonator architecture used in cQED experiments that is designed to address challenges related to losses, cross-talk, and packaging that can limit coherence and scalability in planar devices. Researchers can use this platform to build more intricate circuits with multiple resonators and qubits. In the near term, it allows for significantly more complex, many-resonator, many-qubit circuits^{47,48}.
- **3D cavities:** a resonant structure with a cylindrical geometry, supporting standing electromagnetic waves at specific frequencies determined by its dimensions and boundary conditions. In cQED, these cavities are vital for creating and manipulating quantum coherence, coupling superconducting qubits to microwave photons, facilitating efficient quantum state transfer, implementing

error correction protocols, and simulating quantum systems^{49,50}.

- **CPW resonators:** integral to cQED experiments, utilize coplanar waveguide structures to support standing electromagnetic waves at specific frequencies determined by their dimensions and boundary conditions. Fabricated with superconducting materials like niobium or aluminum, CPW resonators consist of a central conductor, ground planes, and a dielectric layer. Their applications include creating and maintaining quantum coherence, coupling qubits to microwave photons, manipulating quantum states, and implementing error correction protocols⁵¹.

V. TRANSMONS

The journey toward a fault-tolerant quantum computer began with the first experimental demonstrations of superconducting qubits at the turn of the millennium. These pioneering designs included the charge qubit, or “Cooper-pair box”⁵², and the flux qubit, which relied on quantum tunneling of charge and magnetic flux, respectively⁵³. While foundational, these early qubits suffered from short coherence times due to a strong sensitivity to environmental noise — predominantly charge noise for the charge qubit and flux noise for the flux qubit. The development of subsequent qubit designs was therefore largely driven by the goal of mitigating these decoherence channels.

The transmon is a type of superconducting qubit developed to minimize sensitivity to charge noise. Originating from Yale University in 2007²², it is based on the Cooper-pair box design, featuring a Josephson junction shunted by a large parallel capacitor, as depicted in Fig. 6. This shunting capacitor reduces sensitivity to charge noise while maintaining anharmonicity. By increasing the Josephson energy to charging energy ratio, the transmon's energy level spacings become insensitive to offset charge fluctuations.

Furthermore, transmons are essential components in quantum computing, enabling the creation, manipulation, and storage of quantum coherence¹¹. Coupling transmons to resonators facilitates efficient quantum state transfer and gate operations, making them valuable tools for advancing quantum information science and computing⁵⁴.

Overall, the transmon qubit plays a central role in advancing research and applications in cQED by offering long coherence times, tunable resonance frequencies, strong anharmonicity, compatibility with CPW resonators, and scalability for building practical quantum technologies¹¹.

In a practical sense, the transmon is built from an LC circuit by replacing an inductor with a Josephson junction. Nonetheless, the design of the transmon is conceived for an operation regime for a significantly increased ratio of Josephson energy and charging energy E_J/E_C . Furthermore, its charge dispersion decreases exponentially with this ratio²².

For a quantitative description of a transmon, its Hamilto-

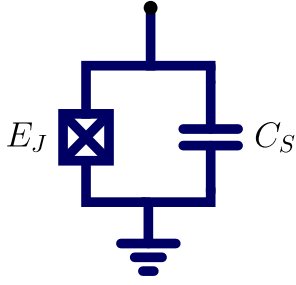


FIG. 6. A transmon qubit represented as a circuit element, consisting of a Josephson junction characterized by its energy E_J shunted by a large capacitor C_S .

nian can be obtained by combining Eqs. (69) and (42):

$$\hat{H} = \frac{\hat{Q}_C^2}{2C} - E_J \cos\left(\frac{\hat{\phi}}{\phi_0}\right) + \frac{\hat{Q}_J^2}{2C_J}, \quad (100)$$

where $\hat{\phi}$ is the flux operator, ϕ_0 is the reduced flux quantum ($\hbar/2e$), \hat{Q}_C^2 is the operator related to the charge accumulated across the capacitor, \hat{Q}_J^2 is the operator related to the charge accumulated across the junction and C_J is the capacitance. Defining $\hat{Q} = \hat{Q}_C + \hat{Q}_J$ and $C_\Sigma = C + C_J$, the Hamiltonian for this quantum system can be expressed as follows:

$$\hat{H} = \frac{\hat{Q}^2}{2C_\Sigma} - E_J \cos\left(\frac{\hat{\phi}}{\phi_0}\right), \quad (101)$$

defining $\hat{n} = \frac{\hat{Q}}{2e}$ and $\hat{\phi} = \frac{\hat{\phi}}{\phi_0}$, and noting that \hat{n} and $\hbar\hat{\phi}$ are conjugated variables:

$$\hat{H} = 4E_C \hat{n}^2 - E_J \cos(\hat{\phi}), \quad (102)$$

where the charging energy E_C is given by $E_C = \frac{e^2}{2C_\Sigma}$, and the Josephson energy E_J is related to the junction's critical current by $E_J = \frac{\hbar I_c}{2e}$ - Eq. (51).

The ratio E_J/E_C is the key parameter that distinguishes a transmon from its predecessor, the Cooper-pair box. In the Cooper-pair box regime ($E_J/E_C \sim 1$), the energy levels have a strong, periodic dependence on the offset charge, a property known as high charge dispersion. This makes the qubit's frequency highly sensitive to environmental charge noise. The innovation of the transmon is to operate in the regime where $E_J/E_C \gg 1$. In this limit, the charge dispersion is exponentially suppressed, meaning the energy levels become nearly flat as a function of offset charge. This greatly reduces the qubit's sensitivity to charge noise, leading to significantly longer coherence times²². In this regime, the flux dispersion $\langle \hat{\phi} \rangle^2$ is low, and the Hamiltonian can be approximated up to the fourth order of $\hat{\phi}$ as:

$$\hat{H} = 4E_C \hat{n}^2 + \frac{E_J}{2} \hat{\phi}^2 - \frac{E_J}{4!} \hat{\phi}^4. \quad (103)$$

In this condition, the transmon behaves like a weakly anharmonic oscillator. Moreover, we introduce the creation \hat{b}^\dagger and

annihilation \hat{b} operators for the elementary energy excitations of the transmon circuit as follows:

$$\hat{\phi} = \left(\frac{2E_C}{E_J}\right)^{1/4} (\hat{b}^\dagger + \hat{b}), \quad (104)$$

$$\hat{n} = \frac{i}{2} \left(\frac{E_J}{2E_C}\right)^{1/4} (\hat{b}^\dagger - \hat{b}). \quad (105)$$

Expressing the Hamiltonian in terms of \hat{b} and \hat{b}^\dagger and applying the Rotating Wave Approximation (RWA), which is a standard method in quantum optics used to neglect fast-oscillating terms that average to zero over the relevant timescales of the system's dynamics⁹, results in the simplified form:

$$\hat{H} = \sqrt{8E_C E_J} \hat{b}^\dagger \hat{b} - \frac{E_C}{12} (\hat{b}^\dagger + \hat{b})^4 \approx \hbar\omega_q \hat{b}^\dagger \hat{b} - \frac{E_C}{2} \hat{b}^\dagger \hat{b}^\dagger \hat{b} \hat{b}, \quad (106)$$

where $\hbar\omega_q = \sqrt{8E_C E_J} - E_C$. The RWA is valid when $\hbar\omega_q \gg \frac{E_C}{4}$, which is easily satisfied in the transmon regime. The last term in Eq. (106) represents a Kerr nonlinearity, with $\frac{E_C}{\hbar}$ acting as the Kerr frequency shift per excitation of the nonlinear oscillator. **Plus, the RWA, as well as the analysis of rotating frames, are discussed in deeper detail in Sec. V B.**

Using the commutation relation $\hat{b}\hat{b}^\dagger = \hat{b}^\dagger\hat{b} + \hat{1}$ and neglecting constants, the Hamiltonian simplifies to:

$$\hat{H} = \hbar \left(\omega_q - \frac{E_C}{2\hbar} \right) \hat{b}^\dagger \hat{b} - \frac{E_C}{2} (\hat{b}^\dagger \hat{b})^2. \quad (107)$$

Furthermore, with the excitation operator written in the basis of Fock states, where k represents the number of excitations in the quantum system, specifically in the Fock state basis:

$$\hat{b}^\dagger \hat{b} = \sum_{k=0}^{\infty} k |k\rangle \langle k|. \quad (108)$$

The Hamiltonian becomes:

$$\hat{H} = \sum_k \left[k\hbar \left(\omega_q - \frac{E_C}{2\hbar} \right) - k^2 \frac{E_C}{2} \right] |k\rangle \langle k|, \quad (109)$$

and, for the first excitation frequency $\omega_{01} = \omega_q - E_C/\hbar$, as the transition $|0\rangle \rightarrow |1\rangle$, the Hamiltonian becomes:

$$\hat{H} = \sum_k \left[k\hbar\omega_{01} - k(k-1) \frac{E_C}{2} \right] |k\rangle \langle k|. \quad (110)$$

When considering only the ground and first excited states, the equation can be further simplified to:

$$\hat{H} = \hbar\omega_{01} |1\rangle \langle 1| = -\frac{\hbar\omega_{01}}{2} \hat{\sigma}_z, \quad (111)$$

where $\hat{\sigma}_z$ is the Pauli-Z matrix.

Finally, from the description above of the transmon, some inferences could be made:

- The general behavior of the transmon relates to a weakly anharmonic oscillator;

- The transmon regime allows the approximation for the operation of the transmon that represents the qubit's number states dispersion;
- The second excitation frequency is $w_{12} = w_{01} - E_C$ relates to the lowering caused by the anharmonicity $\alpha = -E_C$.

A. Transmon-Resonator Coupling

At this point, the building blocks of an operational qubit are set. To accomplish this, a way to allow the qubit to function effectively is presented: transmon-resonator coupling. This occurs because the coupling above provides nonlinearity, tunable energy levels, quantum coherence, and efficient readout. These properties are essential for performing quantum information processing tasks such as qubit manipulation, storage, measurement, and feedback control in quantum algorithms⁵⁵.

Firstly, some fundamental concepts of cQED will be presented for the analysis of the transmon-resonator coupling. Afterward, these principles will be applied to scenarios where a transmon qubit interacts with either a gate voltage or an external oscillator.

The process of circuit analysis can be outlined as follows:

1. Start by applying Kirchhoff's laws, which describe how voltages and currents behave in the circuit;
2. Reduce the number of variables to the minimum necessary;
3. Express the capacitive energies in terms of flux derivatives ($E_C = C\dot{\phi}^2/2$) and inductive/Josephson energies in terms of the flux ($E_I = \phi^2/2L$, $E_J = -E \cos(\phi/\phi_0)$);
4. Formulate the Lagrangian, where capacitive (inductive/Josephson) energies correspond to kinetic (potential) energies;
5. Finally, derive the Hamiltonian using a Legendre transform.

1. Transmon coupled to gate voltage

Now, it will be discussed a transmon qubit coupled to a gate voltage, as shown in Fig. 7.

Following the steps of the analysis, according to Kirchhoff's voltage law:

$$V_g + V_B + V_A = 0 \implies V_g + \dot{\phi}_B + \dot{\phi}_A = 0, \quad (112)$$

where $V_g(t)$ is the classical, time-dependent gate voltage applied externally. The terms V_A and V_B represent the internal voltages of the circuit, which are defined by the time-derivatives of the node fluxes ϕ_A and ϕ_B . Rearranging this gives the relation:

$$\dot{\phi}_B = -\dot{\phi}_A - V_g. \quad (113)$$

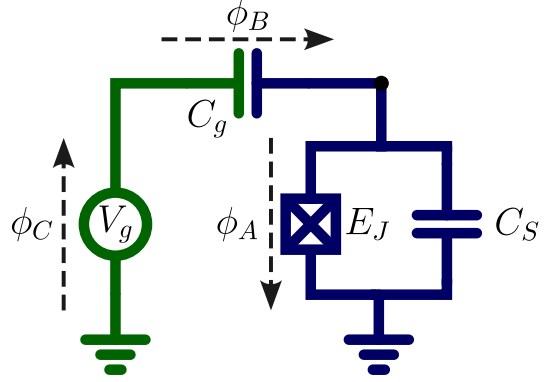


FIG. 7. Representation of a transmon coupled to a gate voltage⁷

The energy stored in the capacitor C_S is $C_S\dot{\phi}_A^2/2$, and in the capacitor C_g is $C_g(\dot{\phi}_A + V_g)^2/2$. The inductive energy of the Josephson Junction is $E_J \cos(\phi_A/\Phi_0)$. Thus, the Lagrangian for this system can be expressed as:

$$\mathcal{L} = \frac{C_S}{2} \dot{\phi}_A^2 + \frac{C_g}{2} (\dot{\phi}_A + \dot{\phi}_C)^2 + E_J \cos(\phi_A), \quad (114)$$

where $E_J = (\phi_0/2\pi)I_c$. The conjugate momentum of ϕ_A is $Q_A = \partial_{\dot{\phi}_A} \mathcal{L} = (C_S + C_g)\dot{\phi}_A + C_g V_g$. The Hamiltonian results from the Legendre transform:

$$H = \dot{\phi}_A Q_A - \mathcal{L}, \quad (115)$$

$$H = \frac{(Q_A - C_g V_g)^2}{2(C_S + C_g)} - E_J \cos\left(\frac{\phi_A}{\phi_0}\right). \quad (116)$$

Expanding the capacitive energy term leads to a drive-transmon interaction term in the form of:

$$\hat{H}_{\text{drive}} = -\frac{C_g Q_{\text{zpf}}}{2(C_S + C_g)} (V_g^* - V_g)(\hat{a}^\dagger - \hat{a}). \quad (117)$$

In the transmon regime, under the RWA:

$$\hat{H}_{\text{drive}} = -\frac{C_g Q_{\text{zpf}}}{2(C_S + C_g)} (V_g \hat{a}^\dagger + V_g^* \hat{a}). \quad (118)$$

From the analysis of Eq. (118), it is possible to arrive at a scenario where the circuit is represented by an operator involving \hat{a} and \hat{a}^\dagger .

Furthermore, the RWA is applied to model the time dependence of $V_g(t)$, where $V_g(t) = \tilde{V}_g e^{-i\omega_d t}$, and ω_d closely matches the resonant frequency of the transmon.

When the quantum behavior of the drives is considered negligible, it is possible to treat the drives as classical forces, significantly easing the mathematical treatment of the system, in what is called the stiff pump regime⁵⁶.

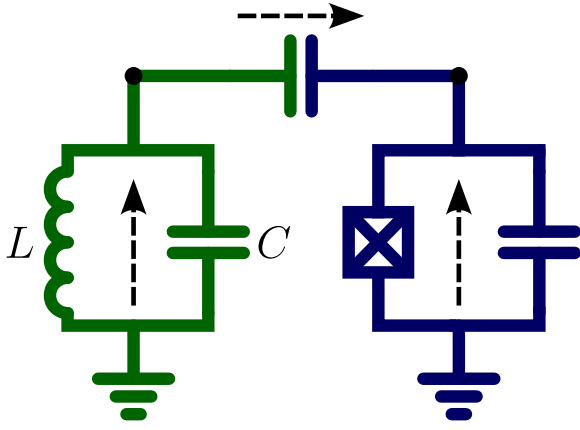


FIG. 8. Representation of a transmon coupled to a resonator, with L and C representing the resonator's inductance and capacitance, respectively.⁷

2. Transmon coupled to resonator

This segment follows the discussion on the transmon coupled to a resonator. The depiction of the aforementioned can be seen in Fig. 8.

Following a method analogous to the previously discussed case of the gate-coupled transmon, the analysis for the capacitive interconnection between a transmon and a resonator begins with Kirchhoff's voltage law. Designating V_1 , V_2 , and V_3 as the voltages across the resonator, gate, and transmon, correspondingly, with orientations structured such that the Kirchhoff voltage law is expressed as:

$$V_1 + V_2 + V_3 = 0. \quad (119)$$

Embracing the flux notation:

$$\dot{\phi}_1 + \dot{\phi}_2 + \dot{\phi}_3 = 0 \implies \dot{\phi}_2 = -\dot{\phi}_1 - \dot{\phi}_3. \quad (120)$$

Reducing the number of variables to the minimum necessary and expressing the capacitive energies in terms of flux derivatives and inductive/Josephson energies, the Lagrangian of this system is delineated as:

$$\mathcal{L} = \frac{C_T}{2} \dot{\phi}_3^2 + \frac{C_R}{2} \dot{\phi}_1^2 + \frac{C_g}{2} (\dot{\phi}_1 + \dot{\phi}_3)^2 + E_J \cos\left(\frac{\phi_3}{\phi_0}\right) - \frac{\phi_1^2}{2L_R}, \quad (121)$$

here, C_g stands for the coupling capacitance, C_R and L_R denote the resonator's capacitance and inductance, respectively, C_T and E_J represent the capacitance and Josephson junction's characteristic energy of the transmon, and ϕ_0 signifies the flux quantum.

The conjugate momenta corresponding to ϕ_1 and ϕ_3 are derived as follows:

$$\begin{cases} Q_1 = \frac{\partial \mathcal{L}}{\partial \dot{\phi}_1} = (C_R + C_g) \dot{\phi}_1 + C_g \dot{\phi}_3 \\ Q_3 = \frac{\partial \mathcal{L}}{\partial \dot{\phi}_3} = (C_T + C_g) \dot{\phi}_3 + C_g \dot{\phi}_1 \end{cases}. \quad (122)$$

Consequently, expressing $\dot{\phi}_1$ and $\dot{\phi}_3$ in terms of Q_1 and Q_3 yields:

$$\begin{cases} \dot{\phi}_1 = \frac{C_T + C_g}{D} Q_1 - \frac{C_g}{D} Q_3 \\ \dot{\phi}_3 = \frac{C_R + C_g}{D} Q_3 - \frac{C_g}{D} Q_1 \end{cases}, \quad (123)$$

where $D = C_R C_T + C_R C_g + C_T C_g$. From the Legendre transform, the Hamiltonian of the system can then be expressed in terms of ϕ_1 , ϕ_3 , Q_1 , and Q_3 :

$$\hat{H} = \dot{\phi}_1 Q_1 + \dot{\phi}_3 Q_3 - \mathcal{L} = \hat{H}_T + \hat{H}_R + \hat{H}_g. \quad (124)$$

Here, \hat{H}_T , \hat{H}_R , and \hat{H}_g signify the transmon, resonator, and coupling terms, respectively, defined as (noting that $Q = 2en$):

$$\hat{H}_T = (4e^2) \frac{C_R + C_g}{2D} \hat{n}_T^2 - E_J \cos \varphi_T, \quad (125)$$

$$\hat{H}_R = (4e^2) \frac{C_T + C_g}{2D} \hat{n}_R^2 + \frac{\phi_0^2}{2L_R} \varphi_R^2, \quad (126)$$

$$\hat{H}_g = -(4e^2) \frac{C_g}{D} \hat{n}_T \hat{n}_R. \quad (127)$$

These equations represent the Hamiltonian terms for different components in the system, where a transmon is coupled to a resonator. Analyzing these equations, some inferences can be made:

- \hat{H}_T is the Hamiltonian term associated with the transmon, which relates to the charging energy of the transmon due to its capacitance with the resonator and gate and the Josephson energy of the transmon;
- \hat{H}_R represents the Hamiltonian term associated with the resonator, which relates to the charging energy of the resonator due to its capacitance with the transmon and gate and the kinetic energy of the resonator;
- \hat{H}_g signifies the Hamiltonian term associated with the coupling between the transmon and the resonator, which represents their interaction due to their capacitive coupling;
- \hat{n}_T and \hat{n}_R represent charge number operators for the transmon and for the resonator, respectively.

Moreover, the negative sign in \hat{H}_g aligns with conventional notation. Expressing the Hamiltonian in terms of creation and annihilation operators \hat{a} , \hat{a}^\dagger , \hat{b} , and \hat{b}^\dagger for the resonator and transmon, respectively, and approximating the cosine function up to the fourth power of the reduced flux, we arrive at:

$$\hat{H} = \hbar \omega_R \hat{a}^\dagger \hat{a} + \hbar \omega_T \hat{b}^\dagger \hat{b} - \frac{E_C}{2} \hat{b}^\dagger \hat{b}^\dagger \hat{b} \hat{b} - \hbar g (\hat{b}^\dagger - \hat{b})(\hat{a}^\dagger - \hat{a}), \quad (128)$$

where ω_R is the resonant angular frequency of the linear LC resonator and ω_T is the transition angular frequency of the transmon qubit. The transmon-resonator coupling constant is determined by the expression:

$$g = \omega_r \frac{C_g}{C_T} \left(\frac{E_J}{2E_C} \right)^{\frac{1}{4}} \sqrt{\frac{\pi Z_R}{2R_K}}, \quad (129)$$

where the terms $Z_R = \sqrt{L_R/C_R}$ and $R_K = h/e^2$ represent the characteristic impedance and quantum resistance, respectively.

It is important to note that the derivation presented here pertains to a scenario involving a single resonator electromagnetic mode. Multiple modes are common in practical setups where the transmon is coupled to a microwave cavity or a transmission line. However, one of these modes is often specifically engineered to exhibit strong coupling with the qubit. Consequently, the weakly interacting modes can be disregarded, simplifying the analysis significantly. However, the study of weakly interacting modes within quantum system environments, such as Feshbach-Fano partitioning⁵⁷, is a field of research with ongoing developments⁵⁸.

B. Rotating frames and approximations

With the coupled Hamiltonian established in Eq. (128), we now turn to the key approximations that enable an analytical solution for the system's dynamics. In regimes typical of transmon-cavity coupling scenarios, certain approximations become applicable, enabling analytical solutions. Commencing with the assumption of the two-level system approximation for the transmon, as described by Eq. (111), the Hamiltonian assumes the form:

$$\hat{H} = \hbar\omega_R \hat{a}^\dagger \hat{a} + \frac{\hbar\omega_T}{2} \hat{\sigma}_z - \underbrace{\hbar g(\hat{\sigma}_+ - \hat{\sigma}_-)(\hat{a}^\dagger - \hat{a})}_{\hat{H}_g}, \quad (130)$$

where \hat{H}_g is the coupling term of the Hamiltonian, and $\hat{\sigma}_+$ and $\hat{\sigma}_-$ are the Pauli raising and lowering operators. Within the two-level approximation, where only the transmon's ground $|0\rangle$ and first excited $|1\rangle$ states are considered, these operators are equivalent to the transmon's creation and annihilation operators, \hat{b}^\dagger and \hat{b} , respectively:

$$\begin{cases} \hat{\sigma}_+ \equiv |1\rangle\langle 0| \approx \hat{b}^\dagger \\ \hat{\sigma}_- \equiv |0\rangle\langle 1| \approx \hat{b} \end{cases}. \quad (131)$$

The initial two terms pertain to the excitation numbers of the resonator and transmon and can be disregarded through the application of a unitary transformation:

$$\hat{U}(t) = \exp\left(-i\omega_R t \hat{a}^\dagger \hat{a} - i\frac{\omega_T t}{2} \hat{\sigma}_z\right), \quad (132)$$

this transformation relocates the problem to an appropriate interaction picture. The two operators summed in the exponent mutually commute, allowing the interpretation of $U(t)$ as a composition of two independent unitary transformations:

$$\hat{U}(t) = \hat{U}_R(t) \hat{U}_T(t) = \hat{U}_T(t) \hat{U}_R(t), \quad (133)$$

with

$$\begin{cases} \hat{U}_T(t) = \exp\left(i\frac{\omega_T t}{2} \hat{\sigma}_z\right), \\ \hat{U}_R(t) = \exp(-i\omega_R t \hat{a}^\dagger \hat{a}). \end{cases} \quad (134)$$

In this newly defined reference frame, the coupling term \hat{H}_g in Eq. (128) undergoes transformation as:

$$\hat{H}_{I,g} = \hat{U}^\dagger(t) \hat{H}_g \hat{U}(t). \quad (135)$$

This defines the dynamics of the system via:

$$i\hbar \frac{\partial}{\partial t} |\psi_i\rangle = \hat{H}_{I,g}(t) |\psi_i\rangle. \quad (136)$$

To comprehend the impact of the coupling Hamiltonian on the evolution of the system's states, it is possible to examine each of the terms of the expansion of the coupling term:

$$\hat{H}_g = -\hbar g(\hat{a} \hat{\sigma}_+ + \hat{a}^\dagger \hat{\sigma}_- - \hat{a}^\dagger \hat{\sigma}_+ - \hat{a} \hat{\sigma}_-). \quad (137)$$

Each component of the interaction Hamiltonian consists of a product of ladder operators associated with the resonator and the transmon, respectively. These operators act on distinct Hilbert spaces and therefore commute, a property that permits the factorization of their action within the full system's tensor product space. As a consequence, any operator confined to the resonator subspace remains invariant under unitary transformations acting solely on the transmon subspace, and vice versa.

This commutation property not only facilitates analytical tractability but also clarifies the nature of the coupling: each term in the Hamiltonian corresponds to a specific excitation exchange process between the two systems. For instance, the presence of a term involving the annihilation operator of the resonator and the creation operator of the transmon explicitly describes the transfer of a single quantum of excitation from the resonator to the transmon. Conversely, a term featuring the resonator's creation operator and the transmon's annihilation operator signifies the reverse process. This structure makes evident the quantized exchange of excitations that underpins the coherent dynamics between the resonator and the transmon.

Thus, computing the transformation detailed in Eq. (136) to elucidate the impact on each ladder operator. Specifically, the transformation of the lowering operator of the cavity is expressed as:

$$\hat{a}_I(t) = \hat{U}^\dagger \hat{a} \hat{U} = \hat{U}_R^\dagger \hat{a} \hat{U}_R \hat{U}_T^\dagger \hat{U}_T, \quad (138)$$

which simplifies to, after expanding in Taylor series:

$$\hat{a}_I(t) = e^{i\omega_R t \hat{a}^\dagger \hat{a}} \hat{a} e^{-i\omega_R t \hat{a}^\dagger \hat{a}} = e^{i\omega_R t \hat{a}^\dagger \hat{a}} \hat{a} \sum_{n=0}^{\infty} \frac{(-i\omega_R t)^n}{n!} (\hat{a}^\dagger \hat{a})^n. \quad (139)$$

Subsequently, using the commutation relation $[\hat{a}, \hat{a}^\dagger] = 1$:

$$\hat{a}(\hat{a}^\dagger \hat{a})^n = (1 + \hat{a}^\dagger \hat{a}) \hat{a} (\hat{a}^\dagger \hat{a})^{n-1} = \dots = (1 + \hat{a}^\dagger \hat{a})^n \hat{a}. \quad (140)$$

Returning the summation to its exponential form, the transformation for the lowering operator of the cavity $\hat{a}_I(t)$ is given by:

$$\hat{a}_I(t) = e^{i\omega_R t \hat{a}^\dagger \hat{a}} \hat{a} e^{-i\omega_R t (1 + \hat{a}^\dagger \hat{a})} \hat{a} = e^{-i\omega_R t} \hat{a}. \quad (141)$$

As anticipated, the transformation for the raising operator is analogously obtained:

$$\hat{a}_I^\dagger(t) = e^{i\omega_R t} \hat{a}^\dagger. \quad (142)$$

The calculation for $\hat{\sigma}_+$ follows a similar procedure, incorporating the commutation rules $[\hat{\sigma}_\pm, \hat{\sigma}_z] = \mp \hat{\sigma}_\pm$, resulting in the expression:

$$\hat{\sigma}_z \hat{\sigma}_\pm = \hat{\sigma}_\pm (\hat{\sigma}_z \pm 1)^n. \quad (143)$$

For the interaction representation, the transformed operators $\hat{\sigma}_{I,\pm}(t)$ are expressed as:

$$\hat{\sigma}_{I,\pm}(t) = e^{\pm i\omega_R t} \hat{\sigma}^\pm. \quad (144)$$

Continuing from the transformations of ladder operators, constructing the transformation of the coupling Hamiltonian from Eq. (135):

$$-\frac{1}{\hbar g} \hat{H}_{I,g} = \hat{a}_I \hat{\sigma}_{I,+} + \hat{a}_I^\dagger \hat{\sigma}_{I,-} - \hat{a}_I^\dagger \hat{\sigma}_{I,+} - \hat{a}_I \hat{\sigma}_{I,-}, \quad (145)$$

$$-\frac{1}{\hbar g} \hat{H}_{I,g} = \hat{a} \hat{\sigma}_+ e^{-i\Delta t} + \hat{a}^\dagger \hat{\sigma}_- e^{i\Delta t} - \hat{a}^\dagger \hat{\sigma}_+ e^{i\Sigma t} - \hat{a} \hat{\sigma}_- e^{-i\Sigma t}, \quad (146)$$

here, $\Delta = \omega_R - \omega_T$ and $\Sigma = \omega_R + \omega_T$. Eq. (146) serves as the initial point for the widely used but infrequently explained Rotating Wave Approximation (RWA). This approximation relies on the observation that when ω_R and ω_T are reasonably close, the last two terms rotate at a high frequency and can thus be neglected from the Hamiltonian.

Returning to the dynamics of the interaction picture (Eq. (136)), expressing the time-dependence of the state as the action of a propagator ($|\psi(t)\rangle = U(t)|\psi_0\rangle$), the resulting equation to solve is:

$$i\hbar \frac{\partial}{\partial t} \hat{U}(t) = \hat{H}_{I,g}(t) \hat{U}(t). \quad (147)$$

Since the interaction Hamiltonian is time-dependent, the propagator does not exhibit a straightforward exponential behavior. Instead, its solution can be attained using the Dyson series:

$$\begin{aligned} \hat{U}(t) = & 1 - i \int_0^t dt_1 \hat{H}_{I,g}(t_1) + \\ & + (-i^2) \int_0^t dt_1 \int_0^{t_1} dt_2 \hat{H}_{I,g}(t_1) \hat{H}_{I,g}(t_2) + \dots \end{aligned} \quad (148)$$

In Eq. (148), the rationale behind the RWA becomes apparent. When a rapidly rotating term is included in the Dyson series, it undergoes integration one or more times before contributing to the state's evolution. Integration acts as a low-pass filter, damping high frequencies. Formally:

$$\int dt e^{i\omega t} = \frac{1}{i\omega} e^{i\omega t} \xrightarrow{\omega \rightarrow \infty} 0. \quad (149)$$

Hence, the last two terms of Eq. (137) can be safely neglected. In fact, the RWA can be applied before transitioning to the interaction picture, yielding the Hamiltonian:

$$\hat{H} = \hbar\omega_R \hat{a}^\dagger \hat{a} + \frac{\hbar\omega_T}{2} \hat{\sigma}_z + \hbar g (\hat{a} \hat{\sigma}_+ + \hat{a}^\dagger \hat{\sigma}_-). \quad (150)$$

The exact diagonalization of this Hamiltonian results in a set of states and eigenenergies denominated Jaynes-Cummings spectrum.

1. Displaced Frame

The concept of a displaced frame offers an alternative approach, steering away from the intricate quantum treatment of an external drive, particularly necessary for input/output theory. A classical drive is typically implemented by coupling a voltage source to the resonator. This interaction is described by a Hamiltonian term $\hat{H}_{\text{drive}} = -\hat{Q}\hat{V}(t)$, where \hat{Q} is the resonator's charge operator and $\hat{V}(t)$ is the classical input voltage. The charge is given by $\hat{Q} \propto i(\hat{a}^\dagger - \hat{a})$, and for a sinusoidal drive at frequency ω_d , the voltage is $V(t) \propto \cos(\omega_d t)$. The interaction term thus contains products like $\hat{a}^\dagger e^{i\omega_d t}$ and $\hat{a} e^{-i\omega_d t}$. By applying the RWA to neglect the fast-oscillating, counter-rotating terms, the total time-dependent Hamiltonian for the driven resonator takes the form:

$$\hat{H}(t) = \hbar\omega_r \hat{a}^\dagger \hat{a} + \hbar(\epsilon_d e^{-i\omega_d t} \hat{a}^\dagger + \epsilon_d^* e^{i\omega_d t} \hat{a}), \quad (151)$$

where ω_r is the resonator frequency, ω_d is the drive frequency, and ϵ_d is the complex amplitude of the drive, encompassing both its strength and phase.

To eliminate the explicit time dependence, we transition to a rotating frame defined by the unitary transformation:

$$\hat{U}(t) = e^{i\omega_d t \hat{a}^\dagger \hat{a}}. \quad (152)$$

The transformed Hamiltonian in this interaction picture is given by:

$$\hat{H}' = \hat{U} \hat{H} \hat{U}^\dagger - i\hbar \hat{U} \frac{d}{dt} \hat{U}^\dagger. \quad (153)$$

Evaluating each term yields:

$$\hat{U} \hat{H} \hat{U}^\dagger = \hbar\omega_r \hat{a}^\dagger \hat{a} + \hbar(\epsilon_d \hat{a}^\dagger + \epsilon_d^* \hat{a}), \quad (154)$$

$$-i\hbar \hat{U} \frac{d}{dt} \hat{U}^\dagger = -\hbar\omega_d \hat{a}^\dagger \hat{a}. \quad (155)$$

Thus, the effective Hamiltonian in the rotating frame becomes:

$$\hat{H}_{\text{eff}} = \hbar(\omega_r - \omega_d) \hat{a}^\dagger \hat{a} + \hbar(\epsilon_d \hat{a}^\dagger + \epsilon_d^* \hat{a}). \quad (156)$$

This is referred to as an “effective” Hamiltonian because it accurately describes the system's dynamics in the rotating frame, with the fast oscillations at the drive frequency ω_d having been mathematically removed. Let us define the detuning as $\Delta = \omega_r - \omega_d$. The Hamiltonian is a time-independent operator that correctly captures the drive dynamics:

$$\hat{H}_{\text{eff}} = \hbar\Delta \hat{a}^\dagger \hat{a} + \hbar(\epsilon_d \hat{a}^\dagger + \epsilon_d^* \hat{a}). \quad (157)$$

The evolution of the annihilation operator in this frame follows the Heisenberg equation of motion⁵⁹:

$$\frac{d}{dt} \hat{a} = \frac{1}{i\hbar} [\hat{H}_{\text{eff}}, \hat{a}] = \frac{1}{i\hbar} (\hbar\Delta [\hat{a}^\dagger \hat{a}, \hat{a}] + \hbar\epsilon_d [\hat{a}^\dagger, \hat{a}]) = -i\Delta \hat{a} - i\epsilon_d. \quad (158)$$

Within this framework, incorporating losses can be approached in two ways: formulating a Lindblad master equation⁶⁰ encompassing amplitude damping, or simply appending a phenomenological damping term to the Heisenberg equation:

$$\frac{d}{dt}\hat{a} = -i\Delta\hat{a} - \frac{\kappa}{2}\hat{a} - i\varepsilon_d. \quad (159)$$

Here, κ represents the *decay constant*, measured in excitations per unit time.

It is important to note that, while both the phenomenological inclusion of a damping term in the Heisenberg equation and the Lindblad master equation approach aim to describe dissipation, they are not strictly equivalent. The Lindblad formalism stems from a rigorous treatment of open quantum systems under the Born-Markov and secular approximations, ensuring complete positivity and trace preservation of the density matrix. In contrast, appending a decay term directly to the Heisenberg equation is a heuristic method that, although often accurate in the semiclassical or weak-damping regimes, may fail to capture certain quantum statistical correlations and non-Markovian effects present in a fully quantum description.

The essence of the displaced frame resides in absorbing the drive ε_d into the definition of \hat{a} . Introducing a classical parameter ξ_d , which obeys the same equation of motion as the expectation value of $\langle \hat{a} \rangle$:

$$\frac{d}{dt}\xi_d = -i\Delta\xi_d - \frac{\kappa}{2}\xi_d - i\varepsilon_d. \quad (160)$$

The difference between the last two equations yields an equation for a new operator, $\tilde{a} = \hat{a} - \xi_d$:

$$\frac{d}{dt}\tilde{a} = -i\Delta\tilde{a} - \frac{\kappa}{2}\tilde{a}. \quad (161)$$

Notably, in this new “displaced” frame, the drive does not directly influence the mode operators but rather displaces the frame itself. Correspondingly, the associated unitary operation constitutes a displacement:

$$\hat{U}_d(t) = e^{\xi_d(t)\hat{a}^\dagger - \xi_d^*(t)\hat{a}}, \quad (162)$$

whereby, $\hat{U}_d^\dagger \hat{a} \hat{U}_d = \hat{a} - \xi_d = \tilde{a}$. Assuming the drive manifests as a constant pulse at frequency ω_d , the steady-state solution for the displacement parameter is derived as:

$$\xi_d = \frac{-i\varepsilon_d}{\kappa/2 + i(\omega_r - \omega_d)}. \quad (163)$$

This last equation shows the steady-state complex amplitude of the displacement, ξ_d , is determined by the drive amplitude (ε_d), the system’s decay rate (κ), and the detuning between the drive and resonator frequencies ($\omega_d - \omega_r$). Overall, this equation describes the coherent state amplitude of the resonator field in response to the applied drive.

C. Jaynes-Cummings Spectrum

The Hamiltonian represented by Eq. (150) elucidates the interplay between the resonator and transmon systems. Each

term within the Hamiltonian holds significance in terms of the stored excitations within the respective systems. The initial two terms distinctly correspond to the resonator and **qubit** number operators. In contrast, the coupling term delineates a number-conserving exchange of excitations. The constancy of the overall excitation count dictates that transitions or couplings solely transpire among states adhering to this fundamental rule.

The composite state $|n, s\rangle$, where n denotes the number of photons in the resonator mode and $s \in \{g, e\}$ labels the transmon in its ground or excited state, forms a natural basis for describing the coupled dynamics of the system. Under the RWA, **the conservation of the total excitation number allows the Hamiltonian to be effectively** decomposed into an infinite set of decoupled two-level subspaces.

Each subspace, labeled by an integer n , captures the dynamics of a fixed total excitation number $n + 1$ and is governed by an effective Hamiltonian \hat{H}_n defined in the subspace spanned by $\{|n + 1, g\rangle, |n, e\rangle\}$. This reduction relies on the assumption that off-resonant couplings to states such as $|n + 2, g\rangle$ and $|n - 1, e\rangle$ are sufficiently suppressed and can be neglected to leading order. Although, in principle, the interaction Hamiltonian allows transitions between any pair of states differing by a single excitation, energy conservation and the weak coupling regime justify the truncation to nearest-neighbor excitation manifolds. Matrix notation represents as:

$$\hat{H}_n = \begin{pmatrix} \langle n + 1, g | \hat{H} | n + 1, g \rangle & \langle n + 1, g | \hat{H} | n, e \rangle \\ \langle n, e | \hat{H} | n + 1, g \rangle & \langle n, e | \hat{H} | n, e \rangle \end{pmatrix}, \quad (164)$$

which results in an effective Hamiltonian that takes the form:

$$\hat{H}_n = \begin{pmatrix} (n + 1)\omega_R - \frac{1}{2}\omega_T & -g\sqrt{n + 1} \\ -g\sqrt{n + 1} & n\omega_R + \frac{1}{2}\omega_T \end{pmatrix}, \quad (165)$$

where ω_R and ω_T are the bare frequencies of the resonator and transmon, respectively, and g characterizes the coupling strength. This matrix formulation highlights the hybridization between the states $|n + 1, g\rangle$ and $|n, e\rangle$ due to the interaction, leading to dressed eigenstates whose energy splitting depends nonlinearly on the excitation number n .

The associated eigenstates and eigenenergies can be readily derived. Hence, defining the detuning $\delta = \omega_R - \omega_T$, $\Omega_n = 2g\sqrt{n + 1}$, and $\Delta_n = \sqrt{\delta^2 + \Omega_n^2}$. Additionally, introducing the trigonometric functions:

$$\sin(\Theta_n) = \frac{\Omega_n}{\sqrt{(\Delta_n - \delta)^2 + \Omega_n^2}}, \quad (166a)$$

$$\cos(\Theta_n) = \frac{\Delta_n - \delta}{\sqrt{(\Delta_n - \delta)^2 + \Omega_n^2}}. \quad (166b)$$

The higher-energy state $|n, +\rangle$ is defined as:

$$|n, +\rangle = \cos(\Theta_n)|n + 1, g\rangle - \sin(\Theta_n)|n, e\rangle, \quad (167)$$

with an associated energy value of $E_{n,+}$:

$$E_{n,+} = \left(n + \frac{1}{2}\right) \omega_R + \frac{1}{2} \Delta_n. \quad (168)$$

Similarly, the lower-energy state $|n, -\rangle$ is defined as:

$$|n, -\rangle = \sin(\Theta_n) |n+1, g\rangle + \cos(\Theta_n) |n, e\rangle, \quad (169)$$

with an associated energy value of $E_{n,-}$:

$$E_{n,-} = \left(n + \frac{1}{2}\right) \omega_R - \frac{1}{2} \Delta_n. \quad (170)$$

This analytical derivation of the Jaynes-Cummings spectrum illuminates the hybridization of states $|n+1, g\rangle$ and $|n, e\rangle$ within the coupled system. This hybridization leads to mixed states $|n, \pm\rangle$ with an energy split characterized by Δ_n . The contributions of either the transmon or resonator in these hybridized states are quantified by $\sin(\Theta_n)$ and $\cos(\Theta_n)$.

Further examination in various regimes sheds light on the implications of this hybridization. In scenarios where both systems are resonant ($\delta = 0$), $\Omega_n = \Delta_n$, resulting in an even distribution of excitation between the transmon and the cavity. Conversely, in the absence of coupling ($g = 0$), the states directly correlate to the subsystem with higher frequency.

Lastly, when a considerable detuning δ is present in the coupled system, akin to the limit $g \rightarrow 0$, the states exhibit tendencies towards dehybridization. This transition minimizes the exchange of excitations between the transmon and resonator systems. Nevertheless, the population of excitation within each subsystem induces alterations in the other's frequency, recognized as the dispersive shift. This condition of substantial δ is commonly referred to as the dispersive regime, prompting an investigation into the derivation of the effective Hamiltonian for this specific case, **which will be done in Sec. VD 2.**

D. Drives and driven systems

The preceding analysis has focused on resonators, transmons, and the nature of their mutual coupling. However, a comprehensive description of quantum hardware also requires the inclusion of external control and measurement mechanisms, particularly those associated with driven interactions. A driven interaction refers to the coherent modulation of a quantum system's dynamics through an externally applied time-dependent field, typically implemented via a transmission line coupled to the system. Such interactions enable both the initialization and manipulation of quantum states, as well as the extraction of information through measurement protocols.

Although Sec. IV A 3 developed a transmission line model where standing wave modes were quantized, when considering the transmission line as a conduit for control and measurement signals, it is often more appropriate to treat it as a continuum of modes. For this purpose, it is more natural to describe the field in terms of propagating waves, which leads to

a continuous spectrum of modes. This approach differs from the discrete modeling presented earlier, and it is particularly relevant when the transmission line is used to deliver broadband signals or when the interaction with the quantum system is not confined to a single resonant mode. Within this perspective, for the purpose of driving and measuring quantum systems, the transmission line serves as the conduit for control pulses and measurement signals, mediating the exchange of energy and information between the quantum system and the classical control infrastructure. Through this framework, the system's dynamics can be steered by tailored drive fields, thereby enabling precise quantum operations and state readout essential for quantum information processing.

Considering the Hamiltonian for a quantum transmission line presented in Eq. 87 and the resulting flux wave equation in Eq. 90, a form of representing the general solution in terms of propagating waves along the x-axis is:

$$\phi(x, t) = \phi_L \left(t + \frac{x}{v}\right) + \phi_R \left(t - \frac{x}{v}\right). \quad (171)$$

Here, ϕ_L and ϕ_R correspond to left and right-propagating waves along the x-axis.

To write the expressions compactly, let the index $j \in \{L, R\}$ denote the left- and right-propagating modes, and let s_j be a sign factor where $s_L = +1$ and $s_R = -1$. Restricting Eq. (171) to $0 < x < L$, where L is a length arbitrarily large, and assuming periodic boundary conditions, leads to the general solution:

$$\phi_j(t + s_j x/v) = \sum_{n=0}^{\infty} \left[A_{j,n} e^{-i \frac{2n\pi v}{L} (t + s_j x/v)} + A_{j,n}^* e^{i \frac{2n\pi v}{L} (t + s_j x/v)} \right]. \quad (172)$$

Ensuring real values for the flux involves algebraic simplifications and considering the limit $L \rightarrow \infty$, allowing the replacement of the summation with integration, where $\omega_n = 2n\pi v/L$:

$$\phi_j(t + s_j x/v) = \int_0^{\infty} d\omega \left[A_j(\omega) e^{-i\omega(t + s_j x/v)} + A_j^*(\omega) e^{i\omega(t + s_j x/v)} \right]. \quad (173)$$

The charge density, as the canonical conjugate pair of the flux, can be obtained via the relation $\lambda_j = c_0 \partial_t \phi_j$. Explicitly:

$$\lambda_j(t + s_j x/v) = -ic_0 \int_0^{\infty} d\omega \omega \left[A_j(\omega) e^{-i\omega(t + s_j x/v)} - A_j^*(\omega) e^{i\omega(t + s_j x/v)} \right]. \quad (174)$$

Utilizing Eqs. (173) and (174), the Hamiltonian (Eq. 87) can be expressed in terms of the coefficients $A_j(\omega)$ and $A_j^*(\omega)$. The outcome, after promoting the coefficients to operators and absorbing normalization factors, is:

$$\hat{H} = \sum_{j \in \{L, R\}} \int_0^{\infty} d\omega \hbar \omega \hat{A}_j^\dagger(\omega) \hat{A}_j(\omega). \quad (175)$$

Defining bosonic creation operators $\hat{b}_j^\dagger(\omega)$ that are proportional to $\hat{A}_j^\dagger(\omega)$, the Hamiltonian takes the standard form for

a continuum of harmonic oscillators:

$$\hat{H} = \sum_{j \in \{L,R\}} \int_0^\infty d\omega \hbar \omega \hat{b}_j^\dagger(\omega) \hat{b}_j(\omega), \quad (176)$$

where the bosonic commutation relations for the operators are assumed: $[\hat{b}_j(\omega), \hat{b}_{j'}^\dagger(\omega')] = \delta_{j,j'} \delta(\omega - \omega')$. The integral can be discretized, allowing the interpretation of the transmission line as a collection of harmonic oscillators with frequencies ω_n :

$$\hat{H} = \sum_{n=0}^\infty \sum_{j \in \{L,R\}} \hbar \omega_n \hat{b}_{j,n}^\dagger \hat{b}_{j,n}. \quad (177)$$

It's noteworthy that for discrete frequencies, $[\hat{b}_{j,n}, \hat{b}_{j',n'}^\dagger] = \delta_{j,j'} \delta_{n,n'}$. Constant offsets to the Hamiltonian were disregarded in both expressions.

Having defined the coefficients $A_j(\omega)$ in terms of bosonic operators, it is possible to reformulate the flux wave expression⁷:

$$\begin{aligned} \phi_j(t + s_j x/v) &= \int_0^\infty d\omega \sqrt{\frac{\hbar}{4\pi\epsilon_0 v}} \left(\hat{b}_j(\omega) e^{-i\omega(t + s_j x/v)} + \hat{b}_j^\dagger(\omega) e^{i\omega(t + s_j x/v)} \right). \end{aligned} \quad (178)$$

From which the voltage expression can also be derived as $V(x, t) = \partial_t \phi(x, t)$:

$$\begin{aligned} V_j(t + s_j x/v) &= -i \int_0^\infty d\omega \sqrt{\frac{\hbar\omega}{4\pi\epsilon_0 v}} \left(\hat{b}_j(\omega) e^{-i\omega(t + s_j x/v)} - \hat{b}_j^\dagger(\omega) e^{i\omega(t + s_j x/v)} \right). \end{aligned} \quad (179)$$

The formulation presented above establishes a quantum field-theoretic model of a transmission line and its coupling to superconducting quantum systems. By recasting the electromagnetic field in terms of propagating bosonic modes, a foundational framework is developed for understanding how external signals induce coherent transitions in qubit-resonator systems. This treatment underpins the theoretical basis for qubit control via microwave drives and paves the way for a quantitative analysis of input-output theory, dissipation, and quantum-limited amplification. The transmission line, therefore, emerges not merely as a conduit for electromagnetic energy, but as a central component in the architecture of scalable quantum information platforms.

1. Drive connected to a quantum system

In the scenario where a transmission line emulates a bath of harmonic oscillators, the coupling of this line to a system of interest can be addressed within the framework of open quantum systems. The analysis of signals transmitted and received through such lines involves the application of input-output theory and the utilization of the Langevin equation, which is a stochastic differential equation that describes how a system

evolves when subjected to a combination of deterministic and fluctuating (random) forces⁶¹.

The standard model for such a setup considers a quantum system of interest coupled to an environment, or “bath”, which is represented as a collection of harmonic oscillators. The complete Hamiltonian describing this entire setup is given by:

$$\hat{H} = \hat{H}_s + \hat{H}_b + \hat{H}_{int}, \quad (180)$$

where each term has a distinct physical meaning. Fully expanded, the Hamiltonian is:

$$\hat{H} = \hat{H}_s + \sum_n \hbar \omega_n \hat{b}_n^\dagger \hat{b}_n + \sum_n \hbar (g_n \hat{a}^\dagger \hat{b}_n + g_n^* \hat{b}_n^\dagger \hat{a}). \quad (181)$$

The three components of the Hamiltonian are interpreted as follows:

- \hat{H}_s is the Hamiltonian for the **system of interest** (e.g., a qubit or transmon) in isolation. It governs the internal energy levels and dynamics of the quantum system itself.
- $\hat{H}_b = \sum_n \hbar \omega_n \hat{b}_n^\dagger \hat{b}_n$ is the Hamiltonian of the **bath**. It models the environment as a collection of independent harmonic oscillators, where \hat{b}_n^\dagger and \hat{b}_n are the creation and annihilation operators for an excitation in the n -th oscillator mode with frequency ω_n .
- $\hat{H}_{int} = \sum_n \hbar (g_n \hat{a}^\dagger \hat{b}_n + g_n^* \hat{b}_n^\dagger \hat{a})$ is the **interaction Hamiltonian**. This term describes the coupling between the system and the bath, allowing for the exchange of energy. It includes terms where the system loses an excitation (via its annihilation operator \hat{a}) while a bath mode gains one (via \hat{b}_n^\dagger), and the corresponding conjugate process. The parameter g_n is the coupling strength between the system and the n -th mode of the bath.

For handling the dynamics of the system, we use the approach of the Langevin equation⁶². A complete derivation of this formalism can be found in Appendix B. This equation describes the time evolution of the system's operators, incorporating both the intrinsic dynamics and the influence of the bath. The Langevin equation for an operator \hat{a} of the system is given by:

$$\frac{d}{dt} \hat{a} = -\frac{i}{\hbar} [\hat{a}, \hat{H}_s] - \frac{\kappa_c}{2} \hat{a} - \sqrt{\kappa_c} \hat{b}_{in}(t). \quad (182)$$

By solving the Heisenberg equations of motion for the bath operators and substituting them back into the equation for \hat{a} , we derive the Langevin equation. Here, κ_c represents the coupling rate between the system and the bath, which quantifies how strongly the system interacts with its environment. The term $\hat{b}_{in}(t)$ is an input operator that encapsulates the influence of incoming signals from the bath on the system. Moreover, from this formalism, it is possible to derive the input-output relations. In the input-output theory, the output operator $\hat{b}_{out}(t)$, which describes the signals leaving the system back into the bath, is related to the input operator and the system operator by:

$$\hat{b}_{out}(t) = \hat{b}_{in}(t) + \sqrt{\kappa_c} \hat{a}(t). \quad (183)$$

While this formulation is general, it can be interpreted in the context of physical systems. If a coupled transmission line simulates the thermal bath, both \hat{b}_{in} and \hat{b}_{out} signify time-dependent signals propagating through the line towards and away from the system of interest. For instance, if the transmission line is defined in the region $0 < x < L$ and linked to a system at $x = 0$, the components \hat{b}_{in}^0 correspond to the operators of left-traveling waves \hat{b}_L as defined earlier. Analogously, the components \hat{b}_{out}^0 refer to the right-traveling modes \hat{b}_R .

Now we will see what happens when a resonator is coupled with a thermal bath. The Hamiltonian that describes the resonator $\hat{H}_s = \hbar\omega_r\hat{a}^\dagger\hat{a}$. Eq. (182) then becomes:

$$\frac{d}{dt}\hat{a} = -i\omega_r\hat{a} - \frac{\kappa_c}{2}\hat{a} - \sqrt{\kappa_c}\hat{b}_{in}. \quad (184)$$

This set of linear differential equations can be solved using the Laplace transform to yield:

$$\hat{a}[s] = \frac{1}{s + i\omega_r + \kappa_c/2}\hat{a}(0) - \frac{\sqrt{\kappa_c}}{s + i\omega_r + \kappa_c/2}\hat{b}_{in}[s], \quad (185)$$

where $\hat{a}[s]$ and $\hat{b}_{in}[s]$ represent the s -plane components of the respective time-dependent operators.

The Laplace transform is employed instead of the Fourier transform due to its ability to incorporate initial conditions and capture transient dynamics in causal systems. This is useful for modeling open quantum systems, where decay and relaxation processes dominate. Moreover, it facilitates input-output analysis and stability characterization in the complex frequency domain, making it a natural choice for describing dissipative quantum dynamics. For \hat{b}_{out} :

$$\hat{b}_{out}[s] = \frac{\sqrt{\kappa_c}}{s + i\omega_r + \kappa_c/2}\hat{a}(0) + \frac{s + i\omega_r - \kappa_c/2}{s + i\omega_r + \kappa_c/2}\hat{b}_{in}[s]. \quad (186)$$

The reflection coefficient $R(s)$ of the resonator derived from this equation is, as $\langle\hat{a}(0)\rangle = 0$:

$$R(s) = \frac{\langle\hat{b}_{out}[s]\rangle}{\langle\hat{b}_{in}[s]\rangle} = \frac{s + i\omega_r - \kappa_c/2}{s + i\omega_r + \kappa_c/2}. \quad (187)$$

In the expression for $R(s)$, the numerator and the denominator contain the complex frequency $s = \sigma + i\omega$, which accounts for the dynamics of the system. The imaginary part, ω , represents the frequency of the probe signal, while the real part, σ , represents its exponential decay or growth rate. The term ω_r is the natural resonant frequency of the cavity, and the parameter $\kappa_c/2$ is the damping rate of the resonator due to its coupling to the environment.

Moreover, this coefficient characterizes how the resonator responds to an input signal $\hat{b}_{in}[s]$ by relating the output signal $\hat{b}_{out}[s]$ to the input signal in the Laplace domain. It delineates the reflection coefficient's reliance on the resonant frequency of the cavity. This frequency becomes modifiable when the cavity establishes a dispersive coupling with a transmon, contingent upon the transmon's state. Consequently, the assessment of $R(s)$ proves instrumental in discerning the populated or unpopulated state of the transmon. The main technique to perform this distinction is via dispersive readout, which will be discussed further.

2. Dispersive Readout

In the realm of cQED, dispersive readout stands as a crucial technique for probing and manipulating quantum systems. This approach enables the extraction of information about the state of a quantum system by observing the **state-dependent frequency shift it induces on a readout resonator**.

To model the measurement process, we consider an input signal consisting of a single, coherent microwave tone at a specific probe frequency, ω_s . In the frequency domain, this input field, $\hat{b}_{in}(\omega)$, can be represented as:

$$\hat{b}_{in}(\omega) = \beta_s\delta(\omega - \omega_s), \quad (188)$$

where $\hat{b}_{in}(\omega)$ is the frequency-domain representation of the input field operator previously introduced as $\hat{b}_{in}(t)$. The Dirac delta function enforces that the input field only contains excitations at the single frequency ω_s , and β_s is the classical complex amplitude of the coherent input drive. Its magnitude squared, $|\beta_s|^2$, is proportional to the input power of the microwave tone; using a classical amplitude is justified because a coherent state is the quantum state that most closely resembles a classical field.

The complex voltage conveyed by the transmission line to the resonator's location at $x = 0$ is derived from the positive-frequency part of the voltage operator, $\hat{V}^{(+)}$. Starting from the general expression in Eq. (179) and substituting the single-tone input field yields:

$$\hat{V}^{(+)}(0, t) = -i \int_0^\infty d\omega \sqrt{\frac{\hbar\omega}{4\pi c_0 v}} \hat{b}_{in}(\omega) e^{-i\omega t} \quad (189)$$

$$= -i \sqrt{\frac{\hbar\omega_s}{4\pi c_0 v}} \beta_s e^{-i\omega_s t}. \quad (190)$$

This expression gives the complex amplitude of the voltage signal at frequency ω_s that arrives at the resonator. The physically meaningful relation connects the power of the input signal to this voltage. The average input power P_{in} is given by the photon rate multiplied by the energy per photon, $P_{in} = \hbar\omega_s|\beta_s|^2$. In a transmission line, power is also $P_{in} = V_{rms}^2/Z_0$, where $Z_0 = 1/(v_0 c_0)$ is the characteristic impedance. Equating this gives the fundamental relationship between voltage and the quantum field amplitude:

$$V_{rms} = \sqrt{\hbar\omega_s Z_0} |\beta_s|. \quad (191)$$

This frequency-dependent relation implies that \hat{V} is not directly proportional to \hat{b}_{in} when the input signal comprises a broad spectrum of frequency components. In such cases, each frequency contributes differently to the voltage due to the $\sqrt{\omega}$ dependence, preventing a uniform scaling between $\hat{b}_{in}(t)$ and $\hat{V}(t)$. Only in the narrowband limit, where the frequency content is sharply peaked around a central frequency ω_s , can the voltage be considered approximately proportional to the input amplitude.

To see how the resonator frequency becomes qubit-state dependent, start from the Jaynes-Cummings Hamiltonian in the

RWA as seen in Eq. (150), with detuning $\Delta \equiv \omega_q - \omega_r$. In the dispersive regime, $|\Delta| \gg g$, energy exchange is suppressed and virtual processes produce state-dependent shifts. Performing a Schrieffer–Wolff transformation^{22,55,63,64} (second-order perturbation theory) with generator

$$\hat{S} = \frac{g}{\Delta} (\hat{a}\hat{\sigma}_+ - \hat{a}^\dagger\hat{\sigma}_-), \quad (192)$$

and transforming \hat{H} to the dispersive frame:

$$\hat{H}_{\text{eff}} \simeq e^{-\hat{S}} \hat{H} e^{\hat{S}} \approx \hat{H} + [\hat{H}, \hat{S}] + \frac{1}{2} [[\hat{H}, \hat{S}], \hat{S}]. \quad (193)$$

By keeping the terms up to order $(g/\Delta)^2$ yields the effective Hamiltonian

$$\hat{H}_{\text{eff}} \simeq \hbar(\omega_r + \chi\hat{\sigma}_z)\hat{a}^\dagger\hat{a} + \frac{\hbar}{2}(\omega_q + \chi)\hat{\sigma}_z + \mathcal{O}(g^2\frac{\hat{a}^\dagger\hat{a}}{\Delta^2}), \quad (194)$$

where, to leading order for a two-level qubit, we define the dispersive shift^{22,55}:

$$\chi \approx \frac{g^2}{\Delta}. \quad (195)$$

For a multi-level transmon the expression is modified by the anharmonicity α , giving the commonly used transmon form $\chi \approx g^2\alpha/[\Delta(\Delta + \alpha)]$; Eq. (195) captures the essential dispersive scaling. The term $\chi\hat{\sigma}_z\hat{a}^\dagger\hat{a}$ shows that the resonator frequency is shifted by $\pm\chi$ depending on the qubit state: $\omega_r + \chi$ for $|e\rangle$ and $\omega_r - \chi$ for $|g\rangle$.

From Eq. (194), the Heisenberg equation for the resonator annihilation operator arrives at the operator Langevin equation in the dispersive limit by including the resonator damping and the input–output terms (as in the bare Langevin equation):

$$\frac{d}{dt}\hat{a} = -i(\omega_r + \chi\hat{\sigma}_z)\hat{a} - \frac{\kappa_c}{2}\hat{a} - \sqrt{\kappa_c}\hat{b}_{in}. \quad (196)$$

This equation acts on the joint Hilbert space of the qubit and resonator. To obtain the dynamics of the resonator conditioned on the qubit being in a specific state, $|g\rangle$ or $|e\rangle$, we can project this operator equation onto the respective qubit subspace. Since the Hamiltonian (Eq. 194) is diagonal in the qubit basis (neglecting off-diagonal terms suppressed in the dispersive limit), the dynamics within the $|g\rangle$ and $|e\rangle$ subspaces decouple. Within these subspaces, the qubit operator $\hat{\sigma}_z$ acts as its corresponding eigenvalue: $\hat{\sigma}_z \rightarrow -1$ for the ground state $|g\rangle$ and $\hat{\sigma}_z \rightarrow +1$ for the excited state $|e\rangle$. Defining \hat{a}_g and \hat{a}_e as the resonator annihilation operator conditioned on the qubit being in state $|g\rangle$ or $|e\rangle$ respectively, Eq. (196) separates into two distinct equations:

$$\frac{d}{dt}\hat{a}_{g,e} = -i(\omega_r \mp \chi)\hat{a}_{g,e} - \frac{\kappa_c}{2}\hat{a}_{g,e} - \sqrt{\kappa_c}\hat{b}_{in}, \quad (197)$$

where the upper sign (+) corresponds to the excited state $|e\rangle$ and the lower sign (−) to the ground state $|g\rangle$. Concretely, if one defines the *total* pull between the two qubit states as $2\chi_{\text{tot}}$, then $\chi_{\text{tot}} = \chi$ in Eq. (197) and the alternative form with $\chi/2$ can be obtained by relabeling the parameter accordingly:

$$\frac{d}{dt}\hat{a}_{g,e} = -i\left(\omega_r \mp \frac{\chi}{2}\right)\hat{a}_{g,e} - \frac{\kappa_c}{2}\hat{a}_{g,e} - \sqrt{\kappa_c}\hat{b}_{in}. \quad (198)$$

Upon replacing $\hat{a}_{g,e}$ with $e^{-i\omega_r t}\tilde{a}_{g,e}$, there is a shift to a reference frame where the cavity states exhibit slow rotation:

$$\frac{d}{dt}\tilde{a}_{g,e} = \left(\mp i\frac{\chi}{2} - \frac{\kappa_c}{2}\right)\tilde{a}_{g,e} - \sqrt{\kappa_c}\tilde{b}_{in}(t), \quad (199)$$

Here, $\tilde{b}_{in}(t) = \hat{b}_{in}(t)e^{i\omega_r t}$ now correlates with the baseband signal transmitted to the cavity.

This state-dependent frequency shift is the cornerstone of dispersive readout. By sending a weak probe tone to the resonator and measuring the reflected (or transmitted) signal, one can determine the resonator’s frequency. As illustrated in Fig. 9, the resonator’s reflection spectrum will exhibit a sharp dip (a resonance) at one of two frequencies: $\omega_r - \chi/2$ if the qubit is in the ground state, or $\omega_r + 2\chi$ if the qubit is in the excited state. By probing the system at a frequency strategically chosen between these two peaks, the phase and amplitude of the reflected signal will be maximally different for the two qubit states, allowing for high-fidelity state discrimination.

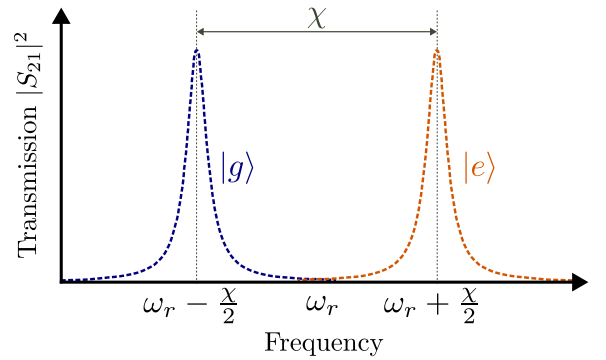


FIG. 9. Illustration of dispersive readout. The resonator’s transmission spectrum (e.g., $|S_{21}|^2$) shows a resonant dip at two different frequencies, separated by χ , depending on whether the qubit is in the ground state $|g\rangle$ (blue) or the excited state $|e\rangle$ (red). A probe tone sent at an intermediate frequency will reflect with a measurably different phase and amplitude for each qubit state.

The dispersive readout protocol is a powerful method for determining the qubit’s state. It leverages the intrinsic dispersive shift—a feature of the Jaynes–Cummings Hamiltonian in the large detuning regime—which causes the resonator’s resonant frequency to change depending on whether the qubit is in its ground or excited state. By probing the resonator with a microwave tone and measuring the reflected signal’s phase and amplitude, one can determine which of the two possible resonant frequencies the resonator has, and thereby infer the state of the qubit. This technique is considered a approximately Quantum Non-Demolition (QND) measurement because, to a good approximation, it measures the qubit’s energy without inducing transitions between $|g\rangle$ and $|e\rangle$. However, this is an idealization; the interaction with readout photons still introduces back action (e.g., dephasing) and will eventually cause the collapse of a superposition state onto one of the energy eigenstates, a fundamental aspect of quantum measurement^{7,8,56}.

VI. APPLICATION EXAMPLE: RABI OSCILLATIONS IN A DRIVEN TRANSMON-RESONATOR SYSTEM

This section consolidates the preceding theoretical concepts by presenting a numerical simulation of a canonical experiment in circuit QED: the observation of vacuum Rabi oscillations. This phenomenon, which represents the coherent exchange of a single quantum of energy between a two-level atom and a cavity mode, serves as a fundamental signature of the strong coupling regime. The simulation will model a driven transmon qubit coupled to a microwave resonator, incorporating the Jaynes-Cummings Hamiltonian, external drives, and the effects of environmental dissipation. The numerical solution of the system's dynamics will be performed using the QuTiP (Quantum Toolbox in Python) library^{65,66}, a standard tool for simulating open quantum systems.

A. System Configuration and Parameters

The physical system consists of a transmon qubit as a **two-level system** coupled to a high-quality factor cavity. Table II summarizes the simulation **parameters used unless otherwise stated**.

TABLE II. Simulation parameters for the transmon–resonator system.

Parameter	Value
Cavity dimension (Fock basis) N	10
Cavity frequency $\omega_R/2\pi$	7.0 GHz
Qubit frequency $\omega_T/2\pi$	5.0 GHz
Coupling strength $g/2\pi$	200 MHz
Cavity decay rate $\kappa/2\pi$	16 MHz
Qubit relaxation rate $\gamma/2\pi$	50 MHz
Bath occupation $\langle n_{th} \rangle$	≈ 0 (10 mK)
Drive amplitude $A/2\pi$	160 MHz
Drive frequency $\omega_d/2\pi$	$\approx \omega_T/2\pi$
Initial state	$ g\rangle \otimes 0\rangle$
Time resolution	256 points

Unless specified, the simulation assumes a dilution-refrigerator environment (~ 10 mK), for which the thermal photon number in the microwave band is negligible, $\langle n_{th} \rangle = [\exp(\hbar\omega_R/k_B T) - 1]^{-1} \approx 0$. The system is initialized in the ground state $|g, 0\rangle$. A transmon-resonant drive at $\omega_d \approx \omega_T$ with amplitude A (Table II) prepares the desired excited-state population; detuning $\Delta = \omega_T - \omega_R$ is then swept to probe resonant and dispersive dynamics.

B. Experimental Protocol and Simulation Scenarios

The protocol explores dynamical regimes by varying coupling strength, dissipation, and detuning, enabling the investigation of coherent and open-system behavior.

The following scenarios are considered:

1. **Baseline System Behavior:** Uncoupled dynamics ($g = 0$) Establishes a baseline by isolating the qubit and cavity evolutions. The addition of the coupling factor adds an energy exchange behavior. Closed versus open dynamics compare unitary evolution to dissipative scenarios incorporating relaxation and photon loss through collapse operators.
2. **Vacuum Rabi Oscillations Measurement:** The energy exchange between qubit, cavity and applied drive is evaluated in terms of a frequency detuning between the qubit and the cavity.

State populations are tracked over time, revealing coherent oscillations, vacuum Rabi splitting, and decoherence mechanisms across different physical regimes.

C. Hamiltonian and Dissipative Dynamics

While the preceding sections used the Heisenberg-Langevin formalism to develop an analytical understanding of input-output theory, for the numerical simulation of the system's full quantum state, it is more convenient to work in the Schrödinger picture. The evolution of the system's density matrix, ρ , is described by the Lindblad master equation^{60,67}, which is the standard and most direct method for this purpose. It provides a complete description of the system's state, including both coherent evolution and incoherent processes like dissipation. This formalism is the cornerstone of numerical solvers for open quantum systems, such as the one implemented in the QuTiP library, making it the natural choice for this simulation.

The coherent evolution of the system is governed by the Jaynes-Cummings Hamiltonian under the RWA. To model the irreversible effects of environmental interaction, such as dissipation and decoherence, the system's evolution is described not by the state vector, but by the density matrix ρ . The dynamics of the density matrix are governed by the Lindblad master equation:

$$\frac{d\rho}{dt} = \frac{1}{i\hbar} [\hat{H}, \rho] + \sum_k \mathcal{D}[L_k] \rho, \quad (200)$$

where the first term describes the unitary evolution and the second term, the dissipator, describes the effects of the environment. Each dissipation channel is represented by a **Lindblad collapse operator**, L_k , where $\mathcal{D}[L_k] \rho = L_k \rho L_k^\dagger - \frac{1}{2} \{L_k^\dagger L_k, \rho\}$.

For the transmon-resonator system, the primary dissipative dynamics include photon loss from the cavity and relaxation of the qubit. These are described by the following collapse operators:

$$L_1 = \sqrt{\kappa(1 + \langle n_{th} \rangle)} \hat{a}; \quad (201a)$$

$$L_2 = \sqrt{\kappa \langle n_{th} \rangle} \hat{a}^\dagger; \quad (201b)$$

$$L_3 = \sqrt{\gamma} \hat{\sigma}_-. \quad (201c)$$

Here, κ is the cavity photon decay rate, γ is the qubit energy relaxation rate, and $\langle n_{th} \rangle$ is the average number of thermal photons in the cavity bath. In the zero-temperature limit ($\langle n_{th} \rangle \rightarrow 0$), the operator L_2 vanishes and only energy decay processes are considered. The presence of L_2 in the finite-temperature case models the absorption of thermal photons from the environment.

Unless otherwise stated, we set the parameters values consistent with Table II. The initial density matrix is $\rho(0) = |g, 0\rangle\langle g, 0|$ (except for the baseline analysis, that $\rho(0) = |g, 1\rangle\langle g, 1|$), and the coherent drive on the transmon is taken in the lab frame at frequency ω_d as in Eq. (202).

D. Measurement

After evolution under each configuration, the occupation probabilities of the transmon and resonator are extracted from the density matrix. These results reveal coherent dynamics, such as vacuum Rabi oscillations, and quantify the impact of detuning and dissipation.

E. Transmon Excitation via Coherent Drive

Excitation of the transmon qubit is modeled through an external coherent drive field, which couples to the qubit's dipole moment and induces Rabi oscillations. This approach reflects experimental protocols in circuit QED, where microwave tones are applied to the system to manipulate its quantum state.

The drive is incorporated into the system Hamiltonian as a time-dependent term of the form:

$$\hat{H}_{\text{drive}} = A \left(e^{-i\omega_d t} \hat{\sigma}_+ + e^{i\omega_d t} \hat{\sigma}_- \right), \quad (202)$$

where A is the drive amplitude, ω_d is the drive frequency, and $\hat{\sigma}_+$ ($\hat{\sigma}_-$) is the raising (lowering) operator acting on the transmon qubit's Hilbert space, treated here as a two-level system. This Hamiltonian describes the interaction of the transmon with a classical field oscillating at frequency ω_d .

Qualitatively, the drive term enables coherent transitions between the ground and excited states of the qubit. When ω_d is resonant or near-resonant with the transmon frequency ω_T , the drive can efficiently induce Rabi oscillations, allowing precise control over the excitation amplitude and duration. The drive amplitude A determines the Rabi frequency, setting the rate at which the qubit undergoes state transitions.

In the simulation protocol, the transmon is initially decoupled from the cavity and driven by the external field until it reaches the desired excited-state population. Following this preparation step, the coupling between the transmon and resonator is activated to investigate energy exchange and coherent dynamics.

F. Simplified Experimental Setup

The simulation proceeds as a standard experimental setup for cQED, directly reflecting the theoretical concepts discussed. At room temperature, an Arbitrary Waveform Generator (AWG) produces precisely shaped baseband pulses, which are mixed with a stable microwave carrier from a Local Oscillator (LO) using an IQ Mixer. This process generates the high-frequency “Drive Signal” used to manipulate the qubit's state, as described by the drive Hamiltonian. This signal is heavily attenuated and sent down into the **dilution refrigerator**, which operates at millikelvin temperatures to prevent thermal noise from destroying the fragile quantum states. Inside, the drive signal interacts with the Qubit-Resonator System. To measure the qubit's state, a separate “Readout Signal” is sent to the resonator. The signal interacts with the system and is reflected, carrying information about the qubit's state via the dispersive shift. This faint reflected signal is then routed back to room temperature, **being amplified along the way** and demodulated by the **readout electronics** to determine the final qubit state, completing the measurement process. **A simplified schematic of this setup is shown in Fig. 10.**

Simplified Experimental Setup for Qubit Control & Readout

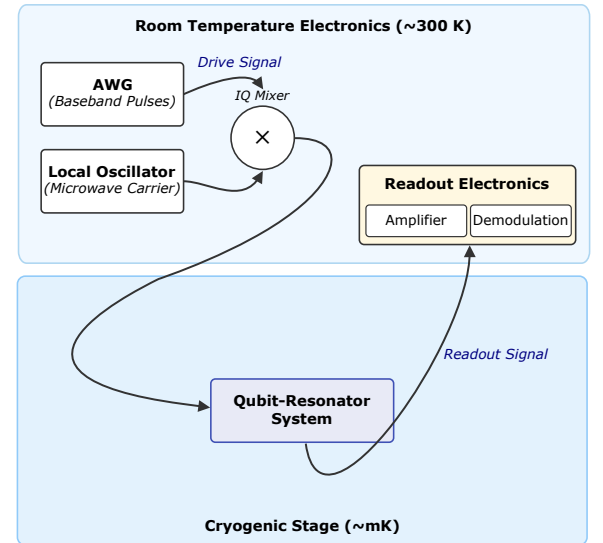


FIG. 10. A simplified schematic of a typical experimental setup for superconducting qubit control and readout. Room-temperature electronics generate and shape microwave pulses (Drive Signal) that are sent into a cryogenic environment to manipulate the state of the Qubit-Resonator System. A separate Readout Signal probes the resonator, and the reflected signal is amplified and processed to measure the qubit's state.

G. System Evolution — Results and Discussion

1. System Baseline Behavior

To build a clear understanding of the coupled system, we first analyze its fundamental dynamics in a simplified, idealized scenario. In this "baseline" simulation, we examine the intrinsic interaction between the qubit and the resonator **without any external drive**.

The goal is to isolate the coherent energy exchange governed by the coupling term, g . To do this, we manually prepare the system in an initial state containing a single quantum of energy. For this specific case, we place the excitation in the cavity, initializing the system in the state $|g, 1\rangle$ (qubit in ground, cavity with one photon). We then observe the subsequent evolution under three conditions: without coupling ($g = 0$), with coupling in a closed system, and with coupling in an open, dissipative system.

It is important to emphasize that this initial state is chosen for pedagogical clarity and does not represent a physical state preparation via a drive, which will be considered in the next section. The results of this analysis are shown in Fig. 11.

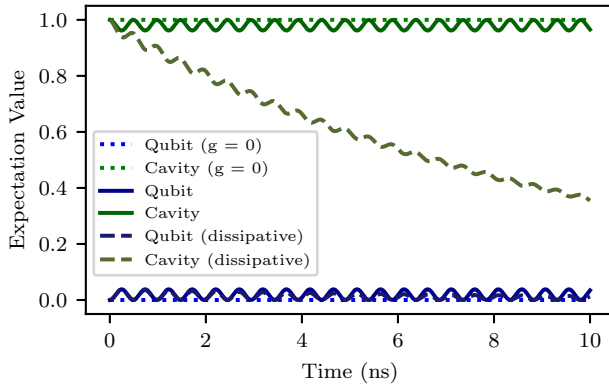


FIG. 11. Expectation values of the qubit and cavity occupation numbers for the baseline analysis. The system is initialized in $|g, 1\rangle$ with no external drive. Solid lines show coherent energy exchange (Rabi oscillations) when coupled ($g \neq 0$). Dotted lines show the uncoupled case ($g = 0$), where the energy remains in the cavity. Dashed lines include dissipation, showing the energy decaying from the system over time.

The results in Fig. 11 illustrate the core behaviors. In the uncoupled case (dotted lines), the cavity population remains at 1 and the qubit at 0, as expected. When coupling is introduced (solid lines), we observe a periodic exchange of energy. Finally, when dissipation is included (dashed lines), the total energy in the system gradually decays.

Notably, the amplitude of the qubit's excitation is very small. This is a direct consequence of the large frequency detuning between the qubit ($\omega_T/2\pi = 5$ GHz) and the resonator ($\omega_R/2\pi = 7$ GHz). With a detuning of $\Delta/2\pi = 2$ GHz, which is much larger than the coupling strength ($|\Delta| \gg g$), the system is in the dispersive regime. In this regime, resonant (real) energy exchange is heavily suppressed. To observe more ef-

ficient and complete energy exchange (i.e., larger amplitude Rabi oscillations), the qubit and resonator would need to be brought close to resonance ($\Delta \approx 0$). Experimentally, this can be achieved by using a flux-tunable qubit, which allows for dynamic modification of its frequency, or by using a cavity projected to have its frequency close to the qubit's frequency.

2. Vacuum Rabi Oscillations Measurement

To model the vacuum Rabi oscillations, we consider the dynamics that occur after the system has been prepared with a single quantum of energy. In a real experiment, this preparation is typically done by applying a brief drive pulse to the qubit (as described by the drive Hamiltonian in Eq. (202)). It is important to remark that we do not need an external drive to observe the vacuum Rabi oscillations themselves. Once energy is inserted into the system, the coherent exchange between the qubit and the cavity due to their coupling will naturally lead to these oscillations.

The system is initialized with the qubit in its ground state and the cavity in its vacuum state, $|g, 0\rangle$. Drive pulses with varying durations are applied to the qubit to excite it, then they are turned off, and the system is allowed to evolve freely under the Jaynes-Cummings Hamiltonian. The detuning $\Delta = \omega_T - \omega_R$ between the qubit and cavity frequencies is swept across a range of values to explore both resonant and off-resonant dynamics. For each detuning and drive duration, the time evolution of the system is computed, and the excited-state population of the qubit is recorded. The resulting interference, shown in Fig. 12, exhibits characteristic chevron-shaped oscillations centered at zero detuning, corresponding to resonant energy exchange between the qubit and the cavity mode. The off-resonant cases show faster but much less complete (lower amplitude) oscillations due to the energy mismatch, as expected from the generalized Rabi frequency expression.

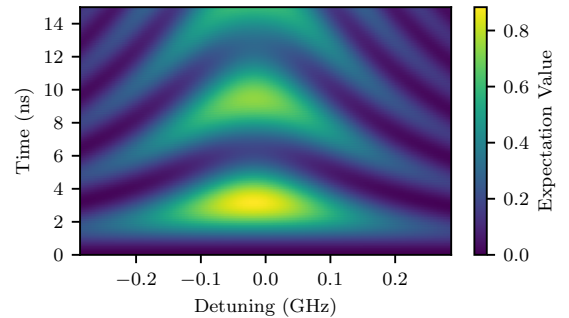


FIG. 12. Vacuum Rabi oscillations as a function of qubit-cavity detuning. Color map of the excited state population of the qubit as a function of interaction time and frequency detuning between the qubit and the resonator. The data reveal the characteristic vacuum Rabi splitting and oscillatory exchange of energy between the qubit and the resonator, with maximum excitation probability occurring at resonance ($\Delta = 0$).

This protocol effectively reveals the coherent nature of light–matter interaction in the cQED regime. Observing such coherent quantum dynamics requires operating in the **strong coupling regime**^{68,69}. This regime is achieved when the coherent coupling rate (g) between the qubit and resonator is much larger than their individual decay rates (κ for the resonator, γ for the qubit), i.e., $g \gg \kappa, \gamma$. Meeting this condition makes possible the reversible exchange of energy between the qubit and resonator multiple times before decoherence occurs, allowing quantum effects to dominate. Achieving strong coupling is therefore a fundamental requirement for building quantum computing platforms based on circuit QED. The observed vacuum Rabi splitting serves as a clear signature of this coherent hybridization, and the dynamics are indicative of fundamental quantum behavior in engineered light–matter systems.

VII. CONCLUSION

This tutorial established a foundation in the principles and applications of superconducting quantum circuits, progressing from fundamental phenomena to advanced quantum electrodynamic architectures. The initial sections elucidated the macroscopic quantum behavior of superconductors, including the Meissner effect and flux quantization, employing both classical and quantum mechanical frameworks. The London equations were derived as essential descriptors of ideal conductivity and perfect diamagnetism, forming the theoretical basis for subsequent quantum device discussions.

A quantum mechanical treatment of the Josephson effect revealed the implications of phase coherence across weak links, with the DC and AC Josephson relations formalizing the interplay between supercurrents, phase differences, and electromagnetic potentials. This framework extended to cQED, detailing the quantization of electromagnetic modes in lumped-element and transmission-line resonators. The formalism demonstrated the function of superconducting resonators as quantum buses for coherent information transfer and infrastructure for qubit coupling.

The transmon qubit was presented as a foundational platform, with its design principles and operational regimes analyzed. By utilizing the nonlinearity of Josephson junctions and mitigating charge noise via large E_J/E_C ratios, transmons achieve enhanced coherence times critical for quantum information processing. The derivation of the transmon-resonator coupling Hamiltonian, complemented by the rotating wave approximation and Jaynes-Cummings model, elucidated mechanisms of coherent energy exchange and state hybridization. Practical considerations, including drive engineering, dissipative dynamics through input-output theory, and dispersive readout techniques, were integrated to connect theoretical constructs with experimental implementations.

Numerical simulation of vacuum Rabi oscillations in a driven transmon-resonator system demonstrated the practical application of these principles. Parameter sweeps across detuning, coupling strength, and dissipation regimes visualized phenomena such as state oscillations and chevron interference

patterns, illustrating the sensitivity of quantum dynamics to Hamiltonian parameters and environmental interactions. This case study reinforced cQED’s capability to emulate and probe light-matter interactions at the quantum level.

The principles and applications of superconducting quantum circuits, as presented, position them as a versatile and scalable platform for quantum information science and technology. The systematic exposition, from macroscopic quantum phenomena to cQED architectures, provides a foundational framework for research and development. The demonstrated capacity for coherent quantum control, along with insights from numerical simulations of light-matter interactions, supports the potential of these engineered quantum systems.

FUNDING

A. J. C. acknowledges partial funding by the Portuguese Foundation for Science and Technology (FCT) in the framework of the Strategic Funding UID/04650/2025.

REFERENCES

- ¹Alessia Pasquazi. A journey through quantum technology. *Journal of Physics: Conference Series*, 2877(1):012077, October 2024.
- ²P. K. Paul, D. Chatterjee, and A. Bhuiamali. *Quantum Information Science Vis-à-Vis Information Schools*, page 4448–4458. IGI Global, 2018.
- ³Alexander M. Dalzell, Sam McArdle, Mario Berta, Przemyslaw Bienias, Chi-Fang Chen, András Gilyén, Connor T. Hann, Michael J. Kastoryano, Emil T. Khabiboulline, Aleksander Kubica, Grant Salton, Samson Wang, and Fernando G. S. L. Brandão. Quantum algorithms: A survey of applications and end-to-end complexities, 2023.
- ⁴M.G.J. Oliveira, T.V.C. Antão, and N.M.R. Peres. The two-site heisenberg model studied using a quantum computer: A didactic introduction. *Revista Brasileira de Ensino de Física*, 46:e20240129, 2024.
- ⁵V. Kumar, S. Gupta, and F.S. Gill. *An overview on quantum computing for technology*, pages 696–701. CRC Press, November 2024.
- ⁶Aishwarya Thomas, Jayant Mahajan, Shalaka Verma, Amit Saxena, Anshul Saxena, and Pritty Jain. Global analysis of quantum technology discourse. In *2024 International Conference on Trends in Quantum Computing and Emerging Business Technologies*, pages 1–6, 2024.
- ⁷Alexandre Blais, Arne L. Grimsom, S. M. Girvin, and Andreas Wallraff. Circuit quantum electrodynamics. *Reviews of Modern Physics*, 93(2), may 2021.
- ⁸P. Krantz, M. Kjaergaard, F. Yan, T. P. Orlando, S. Gustavsson, and W. D. Oliver. A quantum engineer’s guide to superconducting qubits. *Applied Physics Reviews*, 6(2):021318, 06 2019.
- ⁹S. Girvin. *Circuit QED: superconducting qubits coupled to microwave photons*, pages 113–256. 06 2014.
- ¹⁰Britton Plourde and Frank K. Wilhelm-Mauch. *Superconducting Qubits*, pages 719–730. CRC Press, May 2022.
- ¹¹Morten Kjaergaard, Mollie E. Schwartz, Jochen Braumüller, Philip Krantz, Joel I.-J. Wang, Simon Gustavsson, and William D. Oliver. Superconducting qubits: Current state of play. *Annual Review of Condensed Matter Physics*, 11(Volume 11, (2020):369–395, 2020.
- ¹²G. Wendin. Quantum information processing with superconducting circuits: a review. *Reports on Progress in Physics*, 80(10):106001, sep 2017.
- ¹³Liangyu Chen, Hang-Xi Li, Yong Lu, Christopher W. Warren, Christian J. Križan, Sandoko Kosen, Marcus Rommel, Shah Nawaz Ahmed, Amr Osman, Janka Biznárová, Anita Fadavi Roudsari, Benjamin Lienhard, Marco Caputo, Kestutis Grigoras, Leif Grönberg, Joonas Govenius, Anton Frisk Kockum, Per Delsing, Jonas Bylander, and Giovanna Tancredi. Transmon qubit readout fidelity at the threshold for quantum error correction without a quantum-limited amplifier. *npj Quantum Information*, 9(1), March 2023.

- ¹⁴Akash Chohan. A comparative review of quantum bits: Superconducting, topological, spin, and emerging qubit technologies. October 2024.
- ¹⁵Benjamin Rempfer and Kevin Obenland. Comparison of superconducting nisq architectures, 2024.
- ¹⁶C Thomas, J-P Michel, E Deschaseaux, J Charbonnier, R Souil, E Vermande, A Campo, T Farjot, G Rodriguez, G Romano, F Gustavo, B Jadot, V Thiny, Y Thonnart, G Billiot, T Meunier, and M Vinet. Superconducting routing platform for large-scale integration of quantum technologies. *Materials for Quantum Technology*, 2(3):035001, August 2022.
- ¹⁷Christiane P. Koch, Ugo Boscain, Tommaso Calarco, Gunther Dirr, Stefan Filipp, Steffen J. Glaser, Ronnie Kosloff, Simone Montangero, Thomas Schulte-Herbrüggen, Dominique Sugny, and Frank K. Wilhelm. Quantum optimal control in quantum technologies. strategic report on current status, visions and goals for research in europe. *EPJ Quantum Technology*, 9(1):19, Jul 2022.
- ¹⁸H. Kamerlingh Onnes. “*The liquefaction of helium.*”, pages 164–187. Springer Netherlands, Dordrecht, 1991.
- ¹⁹CERN. Cryogenics: Low temperatures, high performance, 2023.
- ²⁰Carsten Timm. Theory of superconductivity, 2020. Version: March 24, 2023.
- ²¹Frank S. Henyey. Distinction between a perfect conductor and a superconductor. *Phys. Rev. Lett.*, 49:416–416, Aug 1982.
- ²²Jens Koch, Terri M. Yu, Jay Gambetta, A. A. Houck, D. I. Schuster, J. Majer, Alexandre Blais, M. H. Devoret, S. M. Girvin, and R. J. Schoelkopf. Charge-insensitive qubit design derived from the cooper pair box. *Phys. Rev. A*, 76:042319, Oct 2007.
- ²³Alexander P. M. Place, Lila V. H. Rodgers, Pranav Mundada, Basil M. Smitham, Mattias Fitzpatrick, Zhaoqi Leng, Anjali Premkumar, Jacob Bryon, Andrei Vrajitoarea, Sara Sussman, Guangming Cheng, Trisha Madhavan, Harshvardhan K. Babla, Xuan Hoang Le, Youqi Gang, Berthold Jäck, András Gyeenis, Nan Yao, Robert J. Cava, Nathalie P. de Leon, and Andrew A. Houck. New material platform for superconducting transmon qubits with coherence times exceeding 0.3 milliseconds. *Nature Communications*, 12(1):1779, Mar 2021.
- ²⁴Youngkyu Sung, Félix Beaudoin, Leigh M. Norris, Fei Yan, David K. Kim, Jack Y. Qiu, Uwe von Lüpke, Jonilyn L. Yoder, Terry P. Orlando, Simon Gustavsson, Lorenza Viola, and William D. Oliver. Non-gaussian noise spectroscopy with a superconducting qubit sensor. *Nature Communications*, 10(1):3715, Sep 2019.
- ²⁵Y. M. Galperin, B. L. Altshuler, J. Bergli, D. Shantsev, and V. Vinokur. Non-gaussian dephasing in flux qubits due to $1/f$ noise. *Physical Review B*, 76(6), Aug 2007.
- ²⁶Irfan Siddiqi. Engineering high-coherence superconducting qubits. *Nature Reviews Materials*, 6(10):875–891, Oct 2021.
- ²⁷Charles Kittel. *Introduction to Solid State Physics*. Wiley, Hoboken, NJ, 8th edition, 2005.
- ²⁸Chandra M Natarajan, Michael G Tanner, and Robert H Hadfield. Superconducting nanowire single-photon detectors: physics and applications. *Superconductor Science and Technology*, 25(6):063001, apr 2012.
- ²⁹Dipak Patel, Su-Hun Kim, Wenbin Qiu, Minoru Maeda, Akiyoshi Matsumoto, Gen Nishijima, Hiroaki Kumakura, Seyong Choi, and Jung Ho Kim. Niobium-titanium (nb-ti) superconducting joints for persistent-mode operation. *Scientific Reports*, 9, 2019.
- ³⁰M. Tinkham. *Introduction to Superconductivity*. Dover Books on Physics Series. Dover Publications, 2004.
- ³¹W. Meissner and R. Ochsenfeld. Ein neuer effekt bei eintritt der supraleitfähigkeit. *Naturwissenschaften*, 21(44):787–788, Nov 1933.
- ³²C.P. Poole, H.A. Farach, R.J. Creswick, and R. Prozorov. *Superconductivity*. Elsevier Science, 2010.
- ³³Elie W’ishe Sorongane. The classical description of the meissner effect: Theory and applications. *Open Journal of Applied Sciences*, 13(3):275–287, 2023.
- ³⁴R. P. Hudson. *Superfluids: Macroscopic Theory of Superconductivity, Vol. I*. Fritz London. New York: Wiley; London: Chapman & Hall, 1950. *Science*, 113(2938):447–447, Apr 1951.
- ³⁵Bascom S. Deaver and William M. Fairbank. Experimental evidence for quantized flux in superconducting cylinders. *Phys. Rev. Lett.*, 7:43–46, Jul 1961.
- ³⁶R. Doll and M. Näbauer. Experimental proof of magnetic flux quantization in a superconducting ring. *Phys. Rev. Lett.*, 7:51–52, Jul 1961.
- ³⁷J. Bardeen, L. N. Cooper, and J. R. Schrieffer. Theory of superconductivity. *Phys. Rev.*, 108:1175–1204, Dec 1957.
- ³⁸V. L. Ginzburg and L. D. Landau. On the Theory of superconductivity. *Zh. Eksp. Teor. Fiz.*, 20:1064–1082, 1950.
- ³⁹Lev Petrovich Gor’kov. Microscopic derivation of the ginzburg-landau equations in the theory of superconductivity. *Sov. Phys. JETP*, 9(6):1364–1367, 1959.
- ⁴⁰D. N. Basov and T. Timusk. Electrodynamics of high- T_c superconductors. *Rev. Mod. Phys.*, 77:721–779, Aug 2005.
- ⁴¹M. H. Devoret and R. J. Schoelkopf. Superconducting circuits for quantum information: An outlook. *Science*, 339(6124):1169–1174, 2013.
- ⁴²B.D. Josephson. Possible new effects in superconductive tunnelling. *Physics Letters*, 1(7):251–253, 1962.
- ⁴³P. W. Anderson and J. M. Rowell. Probable observation of the josephson superconducting tunneling effect. *Phys. Rev. Lett.*, 10:230–232, Mar 1963.
- ⁴⁴P.W. Anderson. Chapter i the josephson effect and quantum coherence measurements in superconductors and superfluids. volume 5 of *Progress in Low Temperature Physics*, pages 1–43. Elsevier, 1967.
- ⁴⁵Max Born, Werner Heisenberg, and Pascual Jordan. *Zur Quantenmechanik. II. Zeitschrift für Physik*, 35:557–615, 1926. Received 16 Nov 1925 (paper spans pp. 557–615; your page 573 is inside this article).
- ⁴⁶S. Haroche, M. Brune, and J. M. Raimond. From cavity to circuit quantum electrodynamics. *Nature Physics*, 16(3):243–246, Mar 2020.
- ⁴⁷Christopher J. Axline, Matthew J. Reagor, Reinier W. Heeres, Philip Reinhold, Chen Wang, Kevin Shain, Wolfgang Pfaff, Yiwen Chu, Luigi Frunzio, and Robert J. Schoelkopf. An architecture for integrating planar and 3d cqcd devices. *Applied Physics Letters*, 109:042601, 2016.
- ⁴⁸D. Rosenberg, D. Kim, R. Das, D. Yost, S. Gustavsson, D. Hover, P. Krantz, A. Melville, L. Racz, G. O. Samach, S. J. Weber, F. Yan, J. L. Yoder, A. J. Kerman, and W. D. Oliver. 3d integrated superconducting qubits. *npj Quantum Information*, 3(1):42, Oct 2017.
- ⁴⁹Luigi Frunzio, Andreas Wallraff, David Schuster, Johannes Majer, and Robert J. Schoelkopf. Fabrication and characterization of superconducting circuit qed devices for quantum computation. *IEEE Transactions on Applied Superconductivity*, 15:860–863, 2004.
- ⁵⁰Hanhee Paik, D. I. Schuster, Lev S. Bishop, G. Kirchmair, G. Catelani, A. P. Sears, B. R. Johnson, M. J. Reagor, L. Frunzio, L. I. Glazman, S. M. Girvin, M. H. Devoret, and R. J. Schoelkopf. Observation of high coherence in josephson junction qubits measured in a three-dimensional circuit qed architecture. *Phys. Rev. Lett.*, 107:240501, Dec 2011.
- ⁵¹A. Wallraff, D. I. Schuster, A. Blais, L. Frunzio, R.-. S. Huang, J. Majer, S. Kumar, S. M. Girvin, and R. J. Schoelkopf. Strong coupling of a single photon to a superconducting qubit using circuit quantum electrodynamics. *Nature*, 431(7005):162–167, Sep 2004.
- ⁵²Y. Nakamura, Yu. A. Pashkin, and J. S. Tsai. Coherent control of macroscopic quantum states in a single-cooper-pair box. *Nature*, 398(6730):786–788, Apr 1999.
- ⁵³J. E. Mooij, T. P. Orlando, L. Levitov, Lin Tian, Caspar H. van der Wal, and Seth Lloyd. Josephson persistent-current qubit. *Science*, 285(5430):1036–1039, 1999.
- ⁵⁴L. DiCarlo, J. M. Chow, J. M. Gambetta, Lev S. Bishop, B. R. Johnson, D. I. Schuster, J. Majer, A. Blais, L. Frunzio, S. M. Girvin, and R. J. Schoelkopf. Demonstration of two-qubit algorithms with a superconducting quantum processor. *Nature*, 460(7252):240–244, Jul 2009.
- ⁵⁵Alexandre Blais, Ren-Shou Huang, Andreas Wallraff, S. M. Girvin, and R. J. Schoelkopf. Cavity quantum electrodynamics for superconducting electrical circuits: An architecture for quantum computation. *Phys. Rev. A*, 69:062320, Jun 2004.
- ⁵⁶Matthew Reagor. *Introduction to Circuit Quantum Electrodynamics*.
- ⁵⁷Alexander Schuray, Luzie Weithofer, and Patrik Recher. Fano resonances in majorana bound states–quantum dot hybrid systems. *Phys. Rev. B*, 96:085417, Aug 2017.
- ⁵⁸Anton Frisk Kockum, Göran Johansson, and Franco Nori. Decoherence-free interaction between giant atoms in waveguide quantum electrodynamics. *Physical Review Letters*, 120(14), April 2018.
- ⁵⁹J. J. Sakurai and Jim Napolitano. *Modern Quantum Mechanics*. Cambridge University Press, 3 edition, 2020.
- ⁶⁰D. Manzano. A short introduction to the lindblad master equation. *AIP Advances*, 2019.
- ⁶¹Y. Gliklikh. The langevin equation. pages 87–94, 1997.

- ⁶²Paul Langevin. *Sur la théorie du mouvement Brownien*. *Comptes rendus de l'Académie des Sciences*, 146:530–533, 1908.
- ⁶³J. R. Schrieffer and P. A. Wolff. Relation between the anderson and kondo hamiltonians. *Phys. Rev.*, 149:491–492, Sep 1966.
- ⁶⁴Alessandro Ciani, David P. DiVincenzo, and Barbara M. Terhal. *Lecture Notes on Quantum Electrical Circuits*. TU Delft OPEN Books, Jul. 2025.
- ⁶⁵J.R. Johansson, P.D. Nation, and F. Nori. QuTiP: An open-source Python framework for the dynamics of open quantum systems. *Computer Physics Communications*, 183(8):1760–1772, aug 2012.
- ⁶⁶J.R. Johansson, P.D. Nation, and F. Nori. QuTiP 2: A Python framework for the dynamics of open quantum systems. *Computer Physics Communications*, 184(4):1234–1240, apr 2013.
- ⁶⁷G. Lindblad. On the generators of quantum dynamical semigroups. *Communications in Mathematical Physics*, 48(2):119–130, Jun 1976.
- ⁶⁸P. Forn-Díaz, L. Lamata, E. Rico, J. Kono, and E. Solano. Ultrastrong coupling regimes of light-matter interaction. *Rev. Mod. Phys.*, 91:025005, Jun 2019.
- ⁶⁹Serge Haroche. Nobel lecture: Controlling photons in a box and exploring the quantum to classical boundary. *Rev. Mod. Phys.*, 85:1083–1102, Jul 2013.
- ⁷⁰H.R. Khan. Superconductivity. In Robert A. Meyers, editor, *Encyclopedia of Physical Science and Technology (Third Edition)*, pages 235–250. Academic Press, New York, third edition edition, 2003.
- ⁷¹Philip W Anderson. How josephson discovered his effect. *Physics Today*, 23(11):23–29, 1970.
- ⁷²Lin Shu-Kun. Classical and statistical thermodynamics. ashley h. carter. *Entropy: International and Interdisciplinary Journal of Entropy and Information Studies*, 4, 12 2003.
- ⁷³William D. Oliver and Paul B. Welander. Materials in superconducting quantum bits. *MRS Bulletin*, 38(10):816–825, 2013.
- ⁷⁴P. Ehrenfest. *Bemerkung über die angenäherte Gültigkeit der klassischen Mechanik innerhalb der Quantenmechanik*. *Zeitschrift für Physik*, 45(7):455–457, Jul 1927.

Appendix A: Quantum Harmonic Oscillator

The Quantum Harmonic Oscillator (QHO) is one of the most fundamental and exactly solvable models in quantum mechanics. It serves as a cornerstone for understanding a wide range of physical phenomena, as its quadratic potential provides an excellent approximation for the behavior of many systems near a point of stable equilibrium. Applications of the QHO are ubiquitous, including the description of molecular vibrations, lattice phonons in solids, and, most importantly for this context, the quantization of modes of the electromagnetic field. Furthermore, its Hamiltonian, which is composed of a sum of squared conjugate operators, provides the mathematical foundation for the formalism of second quantization and serves as a crucial entry point into quantum field theory⁵⁹.

1. Energy and Important Operators

The simple harmonic oscillator is described by its basic Hamiltonian:

$$\hat{H} = \frac{\hat{p}^2}{2m} + \frac{m\omega^2 \hat{x}^2}{2}, \quad (\text{A1})$$

where ω is the angular frequency of the classical oscillator related to the spring constant k in Hooke's law via $\omega = \sqrt{\frac{k}{m}}$. The operators \hat{x} and \hat{p} are Hermitian. Moreover, the Hamilto-

nian can be factored as:

$$\hat{H} = \hbar\omega \left(\frac{m\omega}{2\hbar} \right) \times \left[\left(\hat{x} + \frac{i\hat{p}}{m\omega} \right) \left(\hat{x} - \frac{i\hat{p}}{m\omega} \right) + \frac{1}{2} \right]. \quad (\text{A2})$$

Furthermore, it is convenient to define two non-Hermitian operators known as the annihilation operator \hat{a} and the creation operator \hat{a}^\dagger :

$$\begin{cases} \hat{a} = \sqrt{\frac{m\omega}{2\hbar}} \left(\hat{x} + \frac{i\hat{p}}{m\omega} \right) \\ \hat{a}^\dagger = \sqrt{\frac{m\omega}{2\hbar}} \left(\hat{x} - \frac{i\hat{p}}{m\omega} \right) \end{cases}. \quad (\text{A3})$$

Using the canonical commutation relations, it is obtained:

$$[\hat{a}, \hat{a}^\dagger] = 1. \quad (\text{A4})$$

Given these relations, it is defined the number operator \hat{N} :

$$\hat{N} = \hat{a}^\dagger \hat{a}, \quad (\text{A5})$$

which is Hermitian. With that, the Hamiltonian can be written as:

$$\hat{H} = \hbar\omega \left(\hat{N} + \frac{1}{2} \right). \quad (\text{A6})$$

That is an important relation between the number operator and the Hamiltonian operator. Since the Hamiltonian \hat{H} is a straightforward function of the number operator \hat{N} , it is possible to, simultaneously, find the eigenvalues of \hat{N} along with those of \hat{H} . The representation of an energy eigenstate of \hat{N} by the value n , such that $\hat{N}|n\rangle = n|n\rangle$, so that n must always be a non-negative whole number. As a consequence:

$$\hat{H}|n\rangle = \left(n + \frac{1}{2} \right) \hbar\omega |n\rangle, \quad (\text{A7})$$

which means that the energy eigenvalues are given by:

$$E_n = \left(n + \frac{1}{2} \right) \hbar\omega. \quad (\text{A8})$$

Some important relations linked to the annihilation and creation operators are:

$$\hat{a}|n\rangle = \sqrt{n}|n-1\rangle, \quad (\text{A9})$$

$$\hat{a}^\dagger|n\rangle = \sqrt{n+1}|n+1\rangle. \quad (\text{A10})$$

These relations imply that when there is the application of the operator \hat{a}^\dagger to the state $|n\rangle$, and similarly of \hat{a} on $|n\rangle$, new states are obtained, that are also eigenstates of the number operator \hat{N} . These new states have their eigenvalues increased

or decreased by one. This change by one corresponds to either adding or removing one unit of quantum energy, which is $\hbar\omega$.

Applying systematically the creation operator \hat{a}^\dagger to the ground state $|0\rangle$ using Eq. (A10), it is possible to construct the eigenstates of both the number operator \hat{N} and the Hamiltonian operator \hat{H} :

$$|n\rangle = \left[\frac{(\hat{a}^\dagger)^n}{\sqrt{n!}} \right] |0\rangle. \quad (\text{A11})$$

Using the orthonormality requirement for these states, the matrix elements are derived for the \hat{a} , \hat{a}^\dagger , \hat{x} and \hat{p} operators:

$$\langle n' | \hat{a} | n \rangle = \sqrt{n} \delta_{n', n-1}, \quad (\text{A12})$$

$$\langle n' | \hat{a}^\dagger | n \rangle = \sqrt{n+1} \delta_{n', n+1}, \quad (\text{A13})$$

$$\begin{aligned} \langle n' | \hat{x} | n \rangle &= \sqrt{\frac{\hbar}{2m\omega}} \times \\ &\times \left(\sqrt{n} \delta_{n', n-1} + \sqrt{n+1} \delta_{n', n+1} \right), \end{aligned} \quad (\text{A14})$$

$$\begin{aligned} \langle n' | \hat{p} | n \rangle &= i \sqrt{\frac{m\hbar\omega}{2}} \times \\ &\times \left(-\sqrt{n} \delta_{n', n-1} + \sqrt{n+1} \delta_{n', n+1} \right). \end{aligned} \quad (\text{A15})$$

These matrix elements allow calculating the expectation values of position and momentum operators in these states, which reveal that the ground state has a minimum uncertainty product, while excited states have larger uncertainty products. These findings satisfy the uncertainty principle and confirm the quantum behavior of the harmonic oscillator.

In addition, the following relations are also important:

$$\hat{x} = \sqrt{\frac{\hbar}{2m\omega}} (\hat{a}^\dagger + \hat{a}), \quad (\text{A16})$$

$$\hat{p} = i \sqrt{\frac{m\hbar\omega}{2}} (\hat{a}^\dagger - \hat{a}). \quad (\text{A17})$$

In the position space, the wave functions can be derived for these states. The ground state's wave function is a Gaussian, and the excited states have different wave functions with larger uncertainties, reflecting their higher energy levels. This demonstrates that the uncertainty principle holds for the harmonic oscillator and provides valuable insights into its quantum behavior. So, for the zero point energy, with $x_0 = \sqrt{\frac{\hbar}{m\omega}}$, some useful relations can be obtained:

$$\langle \hat{x} \rangle = \langle \hat{p} \rangle = 0, \quad (\text{A18})$$

$$\langle \hat{x}^2 \rangle = \frac{\hbar}{2m\omega} = \frac{x_0^2}{2}, \quad (\text{A19})$$

$$\langle \hat{p}^2 \rangle = \frac{\hbar m\omega}{2}. \quad (\text{A20})$$

2. Time Evolution of a Quantum Harmonic Oscillator

For treating the time evolution of the Quantum Harmonic Oscillator, since the Hamiltonian is written in the format:

$$\hat{H} = \frac{\hat{p}^2}{2m} + V(\hat{x}), \quad (\text{A21})$$

it is possible to obtain the relations:

$$\frac{dp_i}{dt} = \frac{1}{i\hbar} [p_i, V(\hat{x})] = -\frac{\partial}{\partial x_i} V(\hat{x}), \quad (\text{A22})$$

$$\frac{dx_i}{dt} = \frac{p_i}{m}. \quad (\text{A23})$$

So, applying Eqs. (A22) and (A23) to the annihilation and creation operators, the following uncoupled differential equations are obtained:

$$\frac{d\hat{a}^\dagger}{dt} = i\omega\hat{a}^\dagger, \quad (\text{A24})$$

$$\frac{d\hat{a}}{dt} = -i\omega\hat{a}, \quad (\text{A25})$$

with solutions:

$$\hat{a}^\dagger(t) = \hat{a}^\dagger(0)e^{i\omega t}, \quad (\text{A26})$$

$$\hat{a}(t) = \hat{a}(0)e^{-i\omega t}. \quad (\text{A27})$$

These solutions imply that the operators \hat{N} and \hat{H} are time-independent. Moreover, using these solutions in combination with Eqs. (A16) and (A17), the time evolution for the position and momentum is determined:

$$\hat{x}(t) = \hat{x}(0) \cos \omega t + \left(\frac{\hat{p}(0)}{m\omega} \right) \sin \omega t, \quad (\text{A28})$$

$$\hat{p}(t) = -m\omega \hat{x}(0) \sin \omega t + \hat{p}(0) \cos \omega t. \quad (\text{A29})$$

3. Coherent States

Consider a simple superposition of the two lowest energy eigenstates of the Quantum Harmonic Oscillator:

$$|c\rangle = c_0|0\rangle + c_1|1\rangle. \quad (\text{A30})$$

The expectation value of $x(t)$ then oscillates as

$$\langle c | \hat{x}(t) | c \rangle = 2 \text{Re}(c_0^* c_1) \sqrt{\frac{\hbar}{2m\omega}} \cos \omega t. \quad (\text{A31})$$

While $\langle c | \hat{x}(t) | c \rangle$ oscillates, a single energy eigenstate does not resemble a classical oscillator—its $\langle x \rangle$ and $\langle p \rangle$ are stationary for any n . This leads to a natural question: can one build a

state that oscillates like a classical wave packet without changing shape? Within this framework, a coherent state is defined by the eigenvalue equation for the non-Hermitian annihilation operator \hat{a} :

$$\hat{a}|\lambda\rangle = \lambda|\lambda\rangle, \quad (\text{A32})$$

where λ generally represents a complex eigenvalue that accomplishes this task. The coherent state boasts several other noteworthy properties⁵⁹:

- When expressed as a superposition of energy (or N) eigenstates,

$$|\lambda\rangle = \sum_{n=0}^{\infty} f(n)|n\rangle, \quad (\text{A33})$$

the distribution of $|f(n)|^2$ relative to n follows a Poisson distribution around some mean value \bar{n} :

$$|f(n)|^2 = \frac{\bar{n}^n}{n!} \exp(-\bar{n}). \quad (\text{A34})$$

- It can be derived by displacing the oscillator ground state by a finite distance;
- It maintains the minimum uncertainty product relation at all instances.

Appendix B: Langevin Equation and Input-Output Theory

Consider a quantum system, represented by the Hamiltonian \hat{H}_s , coupled to a bath of harmonic oscillators, described by the Hamiltonian $\hat{H}_b = \sum_n \hbar \omega_n \hat{b}_n^\dagger \hat{b}_n$. The interaction between the system and the bath is given by $\hat{H}_{sb} = \hbar \sum_n (g_n \hat{a}^\dagger \hat{b}_n + g_n^* \hat{a} \hat{b}_n^\dagger)$, where \hat{a} is the annihilation operator for the system, and \hat{b}_n are the annihilation operators for the bath modes. The system dynamics, approached in the Heisenberg picture, consider the assumption of time-dependent operators $\hat{a}(t)$, $\hat{b}_n(t)$, and the resolution of the respective equations:

$$\frac{d}{dt} \hat{a} = \frac{i}{\hbar} [\hat{H}, \hat{a}], \quad (\text{B1})$$

$$\frac{d}{dt} \hat{b}_n = \frac{i}{\hbar} [\hat{H}, \hat{b}_n]. \quad (\text{B2})$$

For \hat{b}_n , this translates into:

$$\frac{d}{dt} \hat{b}_n = -i\omega_n \hat{b}_n - ig_n^* \hat{a}. \quad (\text{B3})$$

Given the initial condition $\hat{b}_n(t=0) = \hat{b}_n^0$, the solution to the equation of motion is:

$$\hat{b}_n(t) = \hat{b}_n^0 e^{-i\omega_n t} - ig_n^* \int_0^t dt' \hat{a}(t') e^{-i\omega_n(t-t')}. \quad (\text{B4})$$

The initial term describes the unimpeded evolution of the bath modes, while the subsequent term arises due to interaction

with the system. Substituting this solution back into the equation of motion for \hat{a} :

$$\frac{d}{dt} \hat{a} = \frac{i}{\hbar} [\hat{H}_s, \hat{a}] - \sum_n ig_n \hat{b}_n^0 e^{-i\omega_n t} - \sum_n |g_n|^2 \int_0^t dt' \hat{a}(t') e^{-i\omega_n(t-t')}. \quad (\text{B5})$$

Several approximations prove useful in simplifying Eq. (B5). The latter term can be reformulated as:

$$\begin{aligned} \sum_n |g_n|^2 \int_0^t dt' \hat{a}(t') e^{-i\omega_n(t-t')} &= \int_0^t dt' \left[\hat{a}(t') e^{-i\omega_c(t-t')} \right] \times \\ &\times \left[\sum_n |g_n|^2 e^{-i(\omega_n - \omega_c)(t-t')} \right], \end{aligned} \quad (\text{B6})$$

where ω_c serves as a central frequency resonating with the free evolution of $\hat{a}(t)$, aiming to render the first bracket's term a slowly rotating one. The term in the second bracket denotes the kernel:

$$K(t-t_0) = \sum_n |g_n|^2 e^{-i(\omega_n - \omega_c)(t-t_0)}. \quad (\text{B7})$$

This, along with a resolution of unity involving Dirac deltas, equates to:

$$\begin{aligned} K(t-t_0) &= \int_{-\infty}^{\infty} \frac{d\omega}{2\pi} \left[2\pi \sum_n |g_n|^2 \delta(\omega_c + \omega - \omega_n) \right] \times \\ &\times e^{-i(\omega_n - \omega_c)(t-t_0)}. \end{aligned} \quad (\text{B8})$$

The term within brackets in Eq. (B8) can be interpreted as the spectral density of the coupling, which defines a frequency-dependent rate. Let's define this rate as a function of a general frequency ω' :

$$\kappa(\omega') \equiv 2\pi \sum_n |g_n|^2 \delta(\omega' - \omega_n). \quad (\text{B9})$$

This function describes how strongly the system couples to the bath modes at a given frequency ω' . The key simplification, known as the Markov approximation, assumes that the bath's memory is very short and that the coupling strength $\kappa(\omega')$ is essentially constant over the range of frequencies relevant to the system's dynamics.

Therefore, we can approximate $\kappa(\omega')$ by its value at the central frequency of interest, ω_c , and treat it as a constant. This constant, κ_c , represents the effective decay rate of the system into the bath:

$$\kappa(\omega') \approx \kappa(\omega_c) \equiv \kappa_c. \quad (\text{B10})$$

In the given context, κ represents the *rate of transfer of excitations*, akin to Fermi's golden rule. It is used in the approximation where the summation term of Eq. (B9) is approximated as $\kappa(\omega_c + \omega)$, where ω_c is a *central frequency* resonating with the free evolution of $\hat{a}(t)$. This approximation simplifies the calculation and allows for the interpretation of the term as the rate of transfer of excitations.

Another valuable approximation assumes the coupling strength coefficients g_n to be approximately a real constant g .

This assumption is reasonable given the frequencies of interest $\omega_c + \omega \approx \omega_c$. This approximation simplifies the expression for κ_c by assuming that the coupling strength g is roughly constant across the range of frequencies relevant to the system's dynamics.

The condition $\omega_c + \omega \approx \omega_c$ is a central feature of the Markov approximation. It is justified by analyzing the system in a reference frame rotating at the central frequency ω_c . In this frame, the system's operators evolve slowly. A slowly varying function is, by its nature, dominated by low-frequency Fourier components. This means the only significant contributions to the interaction integral come from the Fourier frequency variable ω being close to zero. For these dominant components, approximating the total frequency $\omega_c + \omega$ by ω_c becomes a good and physically motivated simplification. Consequently:

$$\kappa_c = 2\pi \sum_n |g_n|^2 \delta(\omega_c - \omega_n) \approx g^2 \sum_n \delta(\omega_c + \omega_n) = 2\pi g^2 D(\omega_c). \quad (\text{B11})$$

The expression for κ_c encapsulates the effective coupling rate between a quantum system and its surrounding bath of harmonic oscillators. From a microscopic perspective, κ_c is defined as a discrete summation over bath modes weighted by their respective coupling strengths $|g_n|^2$ and constrained by the energy-conserving Dirac delta function $\delta(\omega_c - \omega_n)$, ensuring that only resonant interactions contribute to the energy exchange.

Under the assumption that the coupling coefficients g_n vary slowly with frequency and can be approximated by a constant g , the summation simplifies by substituting $|g_n|^2 \approx g^2$. Moreover, the Dirac delta function enforces resonance and effectively selects modes at frequency ω_c . The summation $\sum_n \delta(\omega_c - \omega_n)$ then defines the spectral density of the bath, $D(\omega_c)$, which quantifies the number of available bath modes at the system frequency.

As a result, the expression reduces to $\kappa_c = 2\pi g^2 D(\omega_c)$, establishing a direct relationship between the effective decay rate, the coupling strength, and the bath's density of states at the resonance frequency. This approximation underpins the Markovian treatment of system-bath interactions and is central to the derivation of input-output theory and Langevin dynamics in quantum optics and circuit QED.

Reverting to Eq. (B8) and assuming $\omega_n - \omega_c = \omega$, it is obtained:

$$K(t-t') = \int_{-\infty}^{\infty} \frac{d\omega}{2\pi} \kappa(\omega_c + \omega) e^{-i\omega(t-t')} \approx \kappa_c \delta(t-t'). \quad (\text{B12})$$

Employing Eq. (B12) in Eq. (B6) yields:

$$\int_0^t dt' \hat{a}(t') e^{-i\omega_c(t-t')} \kappa_c \delta(t-t') = \frac{\kappa_c}{2} \hat{a}, \quad (\text{B13})$$

integrating these approximations into Eq. (B5):

$$\frac{d}{dt} \hat{a} = \frac{i}{\hbar} [\hat{H}_s, \hat{a}] - i \sqrt{\frac{\kappa_c}{2\pi D(\omega_c)}} \sum_n \hat{b}_n^0 e^{-i\omega_n t} - \frac{\kappa_c}{2} \hat{a}, \quad (\text{B14})$$

furthermore, by redefining:

$$\hat{b}_{in}(t) = \frac{i}{\sqrt{2\pi D(\omega_c)}} \sum_n \hat{b}_n^0 e^{-i\omega_n t}, \quad (\text{B15})$$

it is possible to arrive at the known Langevin equation:

$$\frac{d}{dt} \hat{a} = \frac{i}{\hbar} [\hat{H}_s, \hat{a}] - \frac{\kappa_c}{2} \hat{a} - \sqrt{\kappa_c} \hat{b}_{in}, \quad (\text{B16})$$

where \hat{b}_{in} represents an *external drive acting upon the system of interest*. It manifests as the Fourier transform of the harmonic amplitudes \hat{b}_n^0 , and is hence proportional to an applied time-dependent signal. Notably, \hat{b}_{in} remains unaffected by \hat{a} but influences the cavity modes as delineated in the Langevin equation.

If instead of Eq. (B4), it is shown a solution for $\hat{b}_n(t)$ in terms of a final time $t_f > t$:

$$\hat{b}_n(t) = \hat{b}_n^f e^{-i\omega_n(t-t_f)} + i g_n^* \int_t^{t_f} dt' \hat{a}(t') e^{-i\omega_n(t-t')}. \quad (\text{B17})$$

Hence, an alternative form of the Langevin equation:

$$\frac{d}{dt} \hat{a} = \frac{i}{\hbar} [\hat{H}_s, \hat{a}] + \frac{\kappa_c}{2} \hat{a} - \sqrt{\kappa_c} \hat{b}_{out}, \quad (\text{B18})$$

where

$$\hat{b}_{out}(t) = \frac{i}{\sqrt{2\pi D(\omega_c)}} \sum_n \hat{b}_n^f e^{-i\omega_n(t-t_f)}. \quad (\text{B19})$$

By subtracting both forms of the Langevin equation, we obtain the input/output relation:

$$\hat{b}_{out}(t) = \hat{b}_{in}(t) + \sqrt{\kappa_c} \hat{a}(t). \quad (\text{B20})$$